SANDIA REPORT

SAND2012-7991
Unlimited Release
Printed August 2012

Equation of state of argon: experiments on Z, density functional theory (DFT) simulations, and wide-range model

John H. Carpenter, Seth Root, Kyle R. Cochrane, Dawn G. Flicker, and Thomas R. Mattsson

Prepared by
Sandia National Laboratories
Albuquerque, New Mexico 87185 and Livermore, California 94550

Sandia National Laboratories is a multi-program laboratory managed and operated by Sandia Corporation, a wholly owned subsidiary of Lockheed Martin Corporation, for the U.S. Department of Energy's National Nuclear Security Administration under contract DE-AC04-94AL85000.

Issued by Sandia National Laboratories, operated for the United States Department of Energy by Sandia Corporation.

Available to DOE and DOE contractors from
U.S. Department of Energy
Office of Scientific and Technical Information
P.O. Box 62
Oak Ridge, TN 37831

Telephone: (865) 576-8401
Facsimile: (865) 576-5728
E-Mail: reports@adonis.osti.gov
Online ordering: http://www.osti.gov/bridge

Available to the public from
U.S. Department of Commerce
National Technical Information Service
5285 Port Royal Rd
Springfield, VA 22161

Telephone: (800) 553-6847
Facsimile: (703) 605-6900
E-Mail: orders@ntis.fedworld.gov
Online ordering: http://www.ntis.gov/help/ordermethods.asp?loc=7-4-0#online

SAND2012-7991
Unlimited Release
Printed August 2012

Equation of state of argon: experiments on Z, density functional theory (DFT) simulations, and wide-range model

John H. Carpenter[1], Seth Root[2], Kyle R. Cochrane[3], Dawn G. Flicker[2],
and Thomas R. Mattsson[3]
[1]Computational Shock and Multiphysics,
[2]Dynamic Material Properties, and [3]HEDP Theory
Sandia National Laboratories
P.O. Box 5800
Albuquerque, NM 87185-1189

Abstract

Over the last few years, first-principles simulations in combination with increasingly accurate shock experiments at multi-Mbar pressure have yielded important insights into how matter behaves under shock loading. Noble gases like argon are particularly interesting to study as a model system due to the closed shell electronic structure that results in a weak interatomic interaction at normal conditions followed by pronounced ionization and strong interaction under compression. Cryogenic argon is also optically transparent while shocked argon is metallic, displaying a reflective shock front, thus allowing for shock velocity measurement to very high precision. In this report, we present experimental results for shock compression of liquid cryogenic argon to several Mbar using magnetically accelerated flyers on the Z machine, first-principles simulations based on Density Functional Theory, and an analysis of tabular equations of state (EOS) for argon, including a newly developed wide-range EOS model.

Acknowledgment

We sincerely thank the many devoted specialists with Z-Operations who are involved in planning and executing experiments on the Z-machine. We thank the cryogenic team: Andrew Lopez, Keegan Shelton, and Jose Villalva for installing and running the cryostat. We thank Aaron Bowers, Nicole Cofer, and Jesse Lynch for assembling the cryo-targets. We thank Charlie Meyers for running the VISAR diagnostics and Devon Dalton for handling target design.

Contents

Appendix

List of Figures

List of Tables

Nomenclature

AK Anode-cathode

AM05 Armiento Mattsson 2005 exchange correlation functional in DFT.

Ar Argon

CRIS A model system for calculating thermodynamic properties for liquids

DFT Density Functional Theory, a theory based on quantum mechanics employed to calculate thermophysical properties like energy and pressure.

EOS Equation of State, the relation between density, temperature, pressure, and internal energy needed to close the hydrodynamic equations of motion.

FCC or fcc Face Centered Cubic, a common lattice structure for transition metals and noble gas solids.

GPa Giga Pascal (10^9) Pascal

K Kelvin

LANL Los Alamos National Laboratory

LDA Local Density Approximation for the exchange-correlation energy in DFT.

LEOS Livermore Equation of State: an EOS format developed at LLNL.

LLNL Lawrence Livermore National Laboratory

VASP Vienna Ab-Initio Simulation Package

VISAR Velocity Interferometer System for Any Reflector

QMD Quantum Molecular Dynamics - employing a first-principles method like DFT to calculate forces on atoms and propagate them according to Newton's equations.

SESAME An EOS format developed at LANL, the table itself can be of different origin, for example LANL or SNL.

SNL Sandia National Laboratories

TFK Thomas-Fermi-Kirzhnitz model for thermodynamic properties of an electron gas.

Xe Xenon

Z The Z-machine at Sandia National Laboratories.

Chapter 1

Introduction

For decades, precise knowledge of the behavior of elements, compounds, and materials under shock compression was limited to the pressures that could be achieved using guns and high explosives. As a result, very little data existed above 100 GPa (1 Mbar). On the theoretical side, electronic structure methods based on quantum mechanics were applied to calculate energy and pressure as a function of compression for perfect lattices (the so called cold curve) but dynamic simulations at temperature were limited to basic model systems like hard/soft spheres or discrete systems, e.g. Ising models. Therefore, it has been exceedingly challenging to predict the behavior of materials much above 1 Mbar. The difficulty in extrapolating equation of state (EOS) models beyond pressures where experimental or high-fidelity simulation data are available is illustrated in Fig. 1.1. For xenon, EOS models predating our work differ notably above 100 GPa and this behavior is by no means limited to xenon. On the contrary, EOS tables of many other elements and compounds exhibit similar discrepancies when different EOS models are extrapolated beyond the range in density and pressure where data is available.

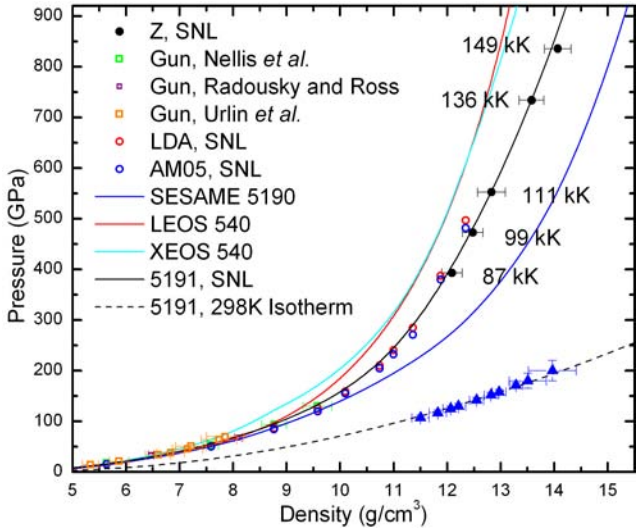

Figure 1.1. Principal Hugoniot for xenon: different tabular EOS models differ significantly above 100 GPa. Our previous work [1] resulted in a new tabular EOS (5191) based on thermodynamic data, DFT/QMD simulations, and multi-Mbar experimental data from Z.

In dramatic contrast to earlier capabilities, over the last few years the combination of increasingly accurate shock experiments at multi-Mbar pressure and first-principles simulations have resulted in greatly improved knowledge of how matter behaves under extreme conditions. For light elements like hydrogen/deuterium [2, 3] and carbon[4] the agreement between simulations and experiments is remarkable, prompting an interest in investigating elements beyond the second row of the periodic table with similar high-fidelity methods.

In earlier work on xenon, we performed density functional theory (DFT) based quantum molecular dynamics (QMD) simulations, high-precision shock experiments, and developed a new tabular equation of state [1]. In this report, continuing a systematic investigation of noble gases, we present results for argon. The behavior of argon is not known experimentally beyond approximately 100 GPa under shock conditions and existing equation of state models differ significantly. We will briefly describe very recent experiments and first-principles simulations aimed at increasing the understanding of argon under high pressure. We will also describe in detail the construction of a wide-range tabular equation of state for argon.

In the first chapter, we present the computational approach for obtaining thermodynamic data from first-principles using DFT. Results from DFT simulations of argon under high-energy density conditions, in particular shock compression, complete the chapter. In chapter two, we describe multi-Mbar shock experiments performed on Sandia's Z machine, including the experimental results for argon. The experimental discussion is followed by a theoretical chapter describing the development of a wide-range equation of state model for argon. The last chapter has concluding remarks.

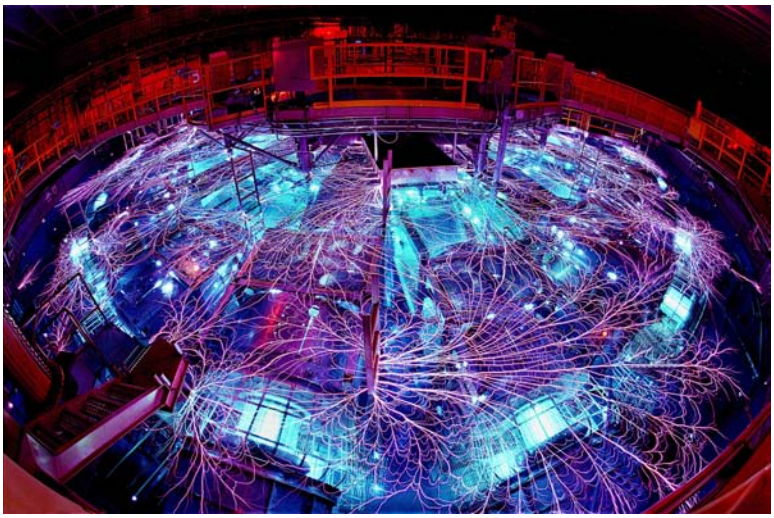

Figure 1.2. One of the main research missions for the Z machine at Sandia National Laboratories is to produce matter under extreme conditions and to measure its properties with high accuracy.

Chapter 2

DFT Simulations of Shocked Argon

Density Functional Theory (DFT) [5, 6] is based on quantum mechanics and is a widely used method to calculate the electronic structure of atoms, molecules, and solids. In DFT, the fundamental property is the density of electrons in three-dimensional real space, $\rho(x,y,z)$, regardless of how many electrons are in the system. This reformulation of the Schrödinger equation from many-body wave-functions to density makes DFT calculations very fast/efficient and it is possible to calculate properties of several hundred atoms.

DFT was for a long time employed in solid-state physics and surface science but its usefulness has with time extended into many other fields of physics. In high-energy density physics (HEDP), the breakthrough came when it was possible to perform high-precision calculations of thermodynamic quantities like internal energy and pressure [3]. Today, DFT is extensively used in HEDP and shock-physics.

The DFT-MD simulations were made with VASP 5.1.40 using projector augmented wave (PAW) core potentials and stringent convergence settings. We employed the standard potential (PAW ArSept2000) at a plane wave cutoff of 600 eV and complex k-point sampling with the mean-value point $(\frac{1}{4},\frac{1}{4},\frac{1}{4})$. Electronic states were occupied according to Mermin's finite-temperature formulation of DFT [7]. We have used two complementary exchange-correlation functionals: the local density approximation (LDA) and the Armiento-Mattsson (AM05) functional. AM05 includes the generalized gradient in addition to the density and is designed to capture the effects of inhomogeneity by matching results for an Airy gas. AM05 has demonstrated high fidelity for wide classes of solids under normal conditions and was recently successfully applied to study quartz to 1.7 TPa under shock compression. The principal Hugoniot is calculated with respect to a given reference state, a density of 1.4 g/cm^3 at 85 K for liquid argon; similar to the experimental initial conditions. The hydrostatic Hugoniot condition is expressed as $2(E-E_{ref}) = (P+P_{ref})(V_{ref}-V)$ with E the internal energy per atom, P the system pressure, V the volume per atom, and the subscript ref denotes a value at the reference state.

The reference simulation used 108 atoms (see Fig. 2.1) and was run for 8 ps to ensure the mean reference pressure and energy were equilibrated to less than 0.5% standard deviation. The average pressure and energy were found using block averaging [8] to reduce correlation, as shown in Fig. 2.2. At low densities and temperatures, the simulations were run for multiple picoseconds at a 1 fs time step. At higher densities and temperatures, this time step was reduced to keep the number of electronic iterations per time step between 4 and 6. We found that if the electronic iteration

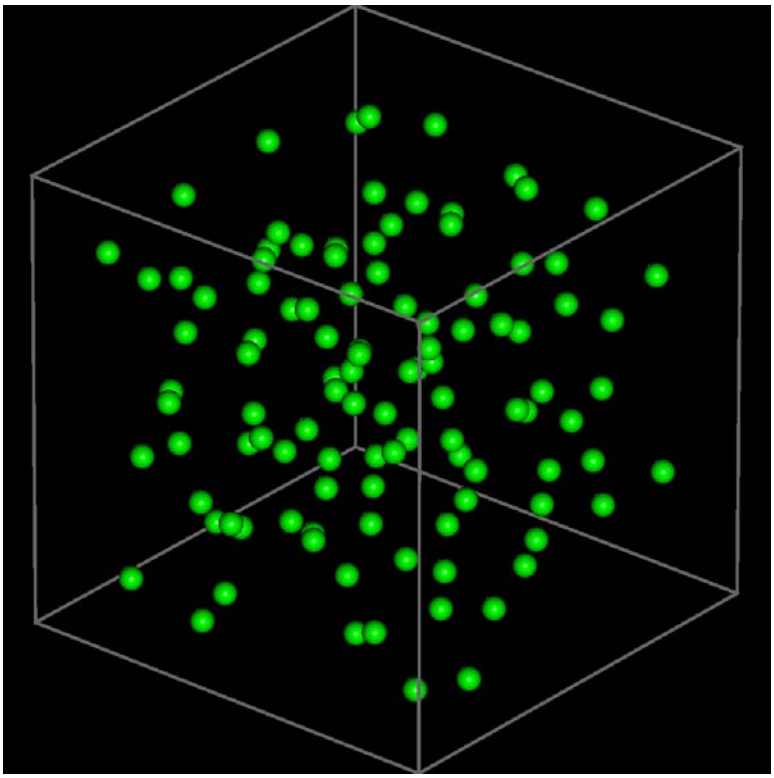

Figure 2.1. Snapshot of a typical DFT-MD simulation with 108 atoms in a periodic rectilinear box.

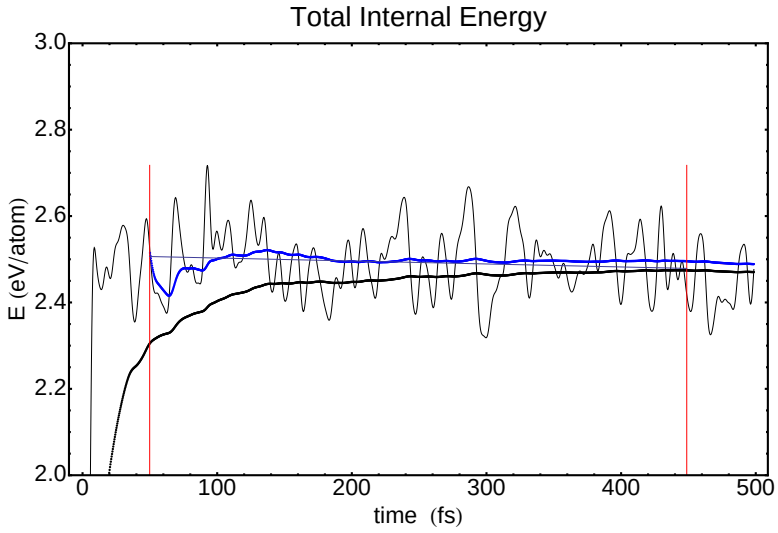

Figure 2.2. The black, highly oscillatory line, is the electronic energy calculated by VASP. The smoother black line is a running average of the energy. The blue line is a cumulative average and the red lines are where the block averaging begins and ends. The cumulative and block averaging start later in time because VASP simulations that are not started with a complete restart (same WAVECAR as well as CONTCAR) have an initial ring and takes some time to begin reaching equilibrium.

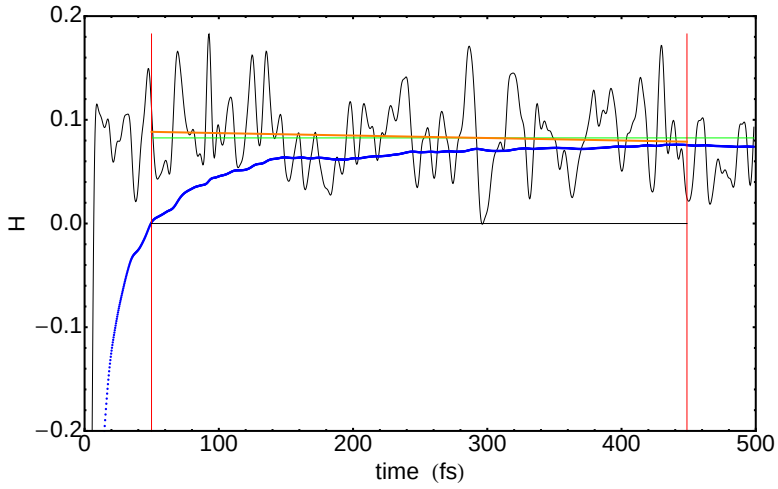

Figure 2.3. Measure of the Rankine-Hugoniot relation. This figure shows the time dependent solving of the Rankine-Hugoniot relation as the simulation approaches a steady-state solution. The highly oscillatory black line is $H = 2(E - E_{ref}) - (P + P_{ref})(V_{ref} - V)$ as a function of time. The blue line is the running average of H. The red lines are the boundaries of the block averaging where the actual mean and block averaging values of H are taken. The green line is mean H. The orange line is the fit to the time dependent H. This is useful if we are ramping the temperature to more quickly find where H=0 is true and also helps determine if we have reached a steady solution based on the magnitude of the slope. The thin black line at 0 is simply to help show if the solution above or below so we know how to adjust the temperature.

count exceeded 8, the simulation would often crash many hundreds of ionic steps later because the ions were allowed to move too far in a single time step and eventually took the simulation to an ill-posed super-cell (a symptom of this is widely oscillating number of electronic iterations).

At each point along the Hugoniot, we would run at least two simulations. The simulations' temperatures were set such that the Hugoniot relation would have one point above and one point below where the Hugoniot relation was true as shown in Fig. 2.3. The actual Hugoniot point would then be interpolated between them. We bracketed the Hugoniot point because extrapolation does not work well especially around phase transitions (melt) as the pressure and energies around are often non-linear. Also, if the temperatures are too far from the Hugoniot point, then the interpolated value can be farther from the actual value than expected. The size of this window is material and Hugoniot location dependent but for most materials, ± 0.1 appears to be maximum. For example, the 1.9 g/cm^3 244 K Hugoniot point was interpolated from a 225 K and 300 K simulation. The 3.9 g/cm^3 simulations were at 22,000 K and 23,000 K. And while this bracket is a bit larger than normal, the simulations showed we were in a gas regime such that it was adequate, primarily because we also ran 20,000 Kelvin and found a 1% difference in the interpolated Hugoniot pressure. When looking for dissociation of polymers, we usually tighten those tolerances to ± 0.01 or less

if possible. At high compression, when the Hugoniot is almost independent of density, we vary the density at a fixed temperature and interpolate in density. In the high density cases, we used 0.1 g/cm^3 initially, but converge to a 0.05 g/cm^3 bracket once we have a good approximation for where the Hugoniot is.

Because the number of bands goes up with temperature thereby increasing the simulation solve time, keeping 108 atoms in the simulation for a clearly gas/liquid regime appeared to be excessive. We reduced the number of atoms to 54 and then 32 and checked the pressure and energy values of the simulation. After twice compressed, we found very little difference between the larger and smaller simulations and so did much of the higher density Hugoniot with 32 atoms. We spot checked occasionally to ensure that simulations with smaller numbers of atoms still matched those with 108.

Because we set the temperature, our simulations are referred to as NVT (fixed number of atoms, volume, and prescribed temperature). One of the other methods available in VASP is NVE (fixed number of atoms, volume, and prescribed energy), but is not used in this case. As such, we can report the temperature used as part of the Hugoniot even though the temperature is not used in the Rankine-Hugoniot relation. We compared two different potentials and found at high pressure they matched, but at lower pressure there was some discrepancy. These results are listed in Tables 2.1 and 2.2. These results were not unanticipated based on the difference in how binding is treated between the two potentials.

Table 2.1. Hugoniot from VASP simulations using the LDA potential.

Density	Temperature	Pressure	Energy
g/cm^3	K	kbar	eV/atom
1.7	108	-1.13	-0.0901196
2.0	301	9.2	-0.049500
2.3	1163	43.6	0.1588
2.5	2597	91.4	0.5077
2.85	7873	239	1.70271
3.2	13690	424	3.42902
3.5	17700	595	5.17995
4.0	24260	932	8.85985
4.2	27343	1112	10.8695
4.5	31846	1354	13.6978
4.7	35575	1569	16.1907
5.0	42061	1933	20.4889
5.6	62323	3158	34.9266
6.0	90770	5051	57.168

Table 2.2. Hugoniot from VASP simulations using the AM05 potential.

Density	Temperature	Pressure	Energy
g/cm^3	K	kbar	eV/atom
1.7	137	13.23	-0.54317
1.8	179	17.2	-0.51723
1.9	244	22.4	-0.48298
2.0	346	29.5	-0.436136
2.85	7650	267	1.46723
3.8	21363	815	6.9761
3.9	22675	888	7.8010
4.0	23947	952	8.61241
5.0	41363	1967	20.4889
5.6	61651	3189	34.8347
6.35	150000	9500	109

Chapter 3

Multi-Mbar shock experiments on Z

The Z-accelerator at Sandia [9] has been used to study properties of shocked materials for over a decade and the approach has been successively refined. Current pulses of up to 26 MA are carefully tailored to produce shock-less acceleration of flyer plates to very high impact velocities. Figure 3.1 shows the experimental setup in the Z machine center-section. The target consists of an asymmetric coaxial load with a 9 mm X 2 mm cathode stalk. The target is asymmetric because the cathode-anode (AK) gap is different on each side (1 mm and 1.4 mm), which allows us to measure two Hugoniot states in one experiment. The cryo-targets are insulated from the load panels using nylon spacers and the targets are held in place using a nylon press piece.

The argon target is viewed schematically in Fig. 3.2. The copper target cell consisted of an alpha-quartz (z-cut) drive plate and an alpha-quartz (z-cut) rear top-hat. All quartz pieces were supplied by Argus International. The space between the quartz windows was filled with high purity argon gas (Matheson Trigas Research Purity $> 99.999\%$) to a pressure of 16.9 PSI. The argon gas was cooled to 85 K using the Type-3 liquid helium reservoir style cryostat [10]. A 14" long, full diameter (0.5") copper cold rod with two standard copper flex links attached the targets to the copper cold finger on the reservoir. A radiation shield cooled with liquid nitrogen was placed around the cold rod. At 85 K, the density of liquid argon is approximately 1.41 g/cm^3 and the index of refraction is approximately 1.23 [11, 12]. The quartz window surfaces were AR (anti-reflection) coated on both surfaces with the interior surfaces matched to the index of liquid argon. An aluminum flyer initially 1 mm in thickness generated the shock wave in the quartz drive plate.

The primary diagnostic for the experiments was velocity interferometry (VISAR) [13]. As shown on the left in Fig. 3.2, when using quartz windows the 532 nm laser for the VISAR passed through the target cell and reflected off the aluminum flyer. A VISAR velocity profile from an argon experiment is shown on the right in Fig. 3.2. The VISAR is able to track the aluminum flyer velocity up to impact on the quartz drive plate. After impact, a shock is produced in the quartz drive plate. At the pressure created by shock wave, the quartz sample melts into a conducting fluid and the velocity of the shock front is measured directly by the VISAR [14] as indicated in the figure. As the shock transits into the liquid argon, the argon undergoes a insulator to metallic transition causing the shock front in the argon to be reflective. The reshock into the rear quartz window also creates a reflective shock front in the quartz, but the reshock data is not discussed in this report.

For the majority of the experiments, the measured quantities are the shock velocity in the quartz

Figure 3.1. Image of the experimental setup at Z. Gas lines and the cold rod from the cryostat are visible in the image.

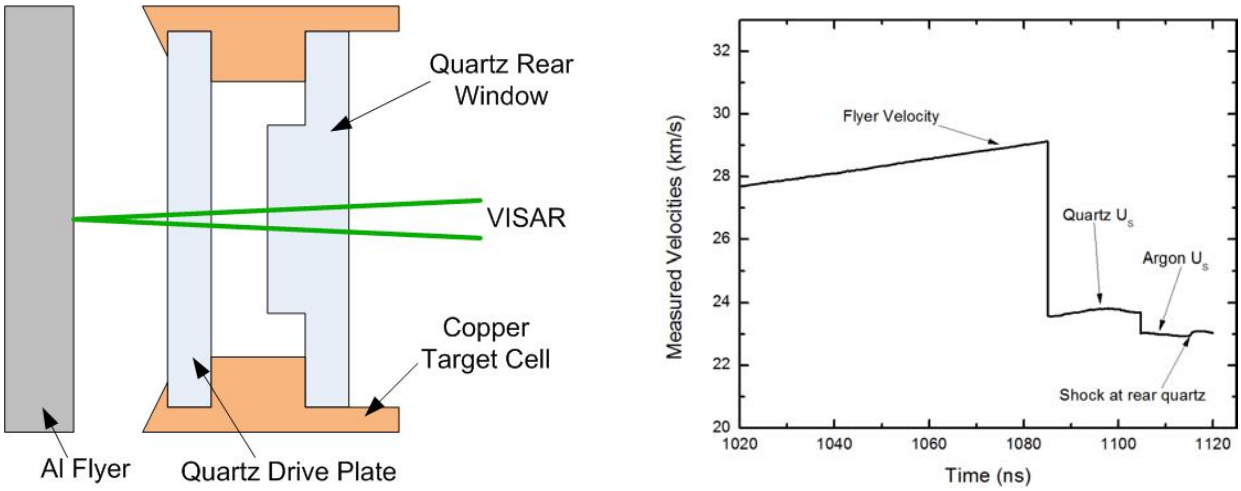

Figure 3.2.
Schematic view of a flyer-plate impact experiment: the flyer approach to the target is measured to high precision using VISAR, the subsequent shock wave fronts are similarly followed in the experiment.

Table 3.1. Cubic fit parameters for the Z-quartz Hugoniot data: $U_S = C_3 U_P^3 + C_2 U_P^2 + C_1 U_P + C_0$

C_3 (s^2/km^2)	C_2 (s/km)	C_1	C_0 (km/s)
$6.979 \times 10^{-4} \pm 3.244 \times 10^{-4}$	-0.03844 ± 0.01031	1.9147 ± 0.1008	1.5591 ± 0.2976

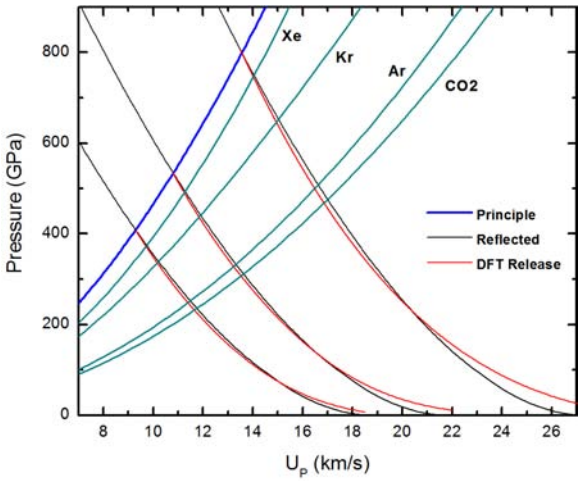

Figure 3.3. Comparison of the reflected Hugoniot and DFT calculated release path for quartz at 3 initial pressure states. $P - U_P$ curves shown for 3 noble gases and CO2 demonstrating the effect of using the reflected Hugoniot versus the release.

drive plate and the shock velocity in the argon sample. The Hugoniot state of the quartz drive plate is determined from the measured shock velocity and a weighted cubic fit to the Z quartz Hugoniot data[14]. The argon Hugoniot state is then determined using *Monte Carlo* Impedance matching methods and the reflected quartz Hugoniot. However, using the reflected quartz Hugoniot produces results that are soft compared to the true response of argon. Thus it is necessary to understand the release path of quartz. The quartz release path has been determined using DFT methods for several points along the Hugoniot and is validated by deep release data [15]. Figure 3.3 shows the quartz release effect compared to the reflected Hugoniot. Argon's low impedance means the reflected versus release effect is greater and needs to be included in the impedance match calculations for accurate results.

The quartz release correction was applied in the following manner:

1. The argon Hugoniot state is calculated using the *Monte Carlo* impedance matching method and the reflected quartz Hugoniot. The quartz Hugoniot is a weighted, cubic fit to the Z experimental data and includes the fit parameter uncertainty and correlation.

2. In $P - U_P$ space, we plot both the quartz reflected Hugoniot and the calculated quartz release path from several known Hugoniot states. Also plotted is the the curve $P = \rho_0 U_S U_P$ where

Table 3.2. Experimental data for the principal Hugoniot of shock compressed liquid argon. The * indicates the experiment was performed with an aluminum drive plate.

Shot	U_P (km/s)	U_S (km/s)	ρ (g/cm^3)	Pressure (GPa)
Z2229-A0174A North	16.48 ± 0.07	21.44 ± 0.05	6.092 ± 0.108	498.1 ± 2.2
Z2233-A0174B North	17.88 ± 0.06	23.01 ± 0.04	6.320 ± 0.092	580.0 ± 2.0
Z2233-A0174B South	18.48 ± 0.06	23.68 ± 0.08	6.427 ± 0.131	617.2 ± 2.5
Z2232-A0174C North*	11.48 ± 0.04	15.73 ± 0.04	5.219 ± 0.071	254.7 ± 1.2
Z2232-A0174C South	12.47 ± 0.05	16.68 ± 0.04	5.582 ± 0.083	293.2 ± 1.4

ρ_0 is the initial density of liquid argon and U_S is the measured value of the shock velocity in argon.

3. From the plot, we calculate the intercepts of the argon curve $P = \rho_0 U_S U_P$ and the reflected and release quartz paths.

4. ΔU_P between the reflected Hugoniot and the release path is determined and a linear fit of the ΔU_P vs. $U_P(reflected)$ is performed.

5. Using the U_P calculated using the reflected Hugoniot and the linear fit calculated above, we can determine the correction to U_P needed to account for the quartz release path. This U_P and the measured U_S are used to calculate the final Hugoniot state pressure and density. The uncertainty in the data does not include the uncertainty in the release path as of this report.

One experimental data point used aluminum as the impedance match standard. The aluminum Hugoniot state was determined from the flyer velocity measured below the cryo-target and the aluminum Hugoniot data from reference [16]. The release state of aluminum into the argon was determined from SESAME 3700. The impedance matching procedure was the same as described above. Table 3.2 lists the experimental results for the principal Hugoniot of liquid argon.

Figures 3.4 and 3.5 show the Z experimental data in the $U_S - U_P$ and $\rho - P$ planes compared with the previous experimental data and the DFT simulation results discussed earlier. In the $U_S - U_P$ plane, the Z experimental data shows lower shock velocities than predicted by the current tabular EOS models. The difference between the tabular EOS models and the experimental data is magnified in the $\rho - P$ plane. The experimental data shows a significantly softer response than predicted by the models. This result was unexpected because previous work on xenon [1] and krypton [17] showed that the earlier tabular EOS models bracketed the true Hugoniot responses. The data point attained using the aluminum drive plate is indicated in the figures. The data point, while consistent with the others, is slightly stiffer than the other Z data points. This scatter is likely caused by the experimental setup as opposed to the liquid argon. In the experiment with the aluminum drive plate, the flyer velocity at impact is determined from a target spot below the cryocell and this velocity is used to determine the Hugoniot state in the aluminum drive plate. Due to target alignment issues, the measured flyer velocity below the cryo-target and the true flyer

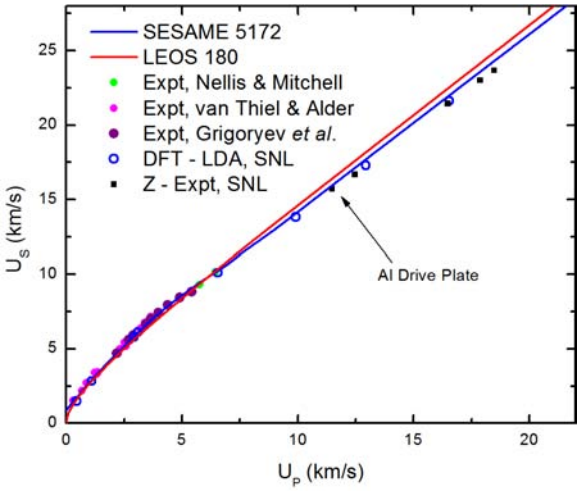

Figure 3.4. $U_S - U_P$ data for argon from previously published results [18–20], DFT-MD calculations, and Z experiments. The existing tabular EOS Hugoniot plots are also shown. For the experimental data, the uncertainty is on the order of the size of the data point.

velocity at the cryo-target can be different up to 1%. This difference was not accounted for in determining the Hugoniot state for Z2232-A0A174C North. Overall, the experimental data clearly demonstrate a softer Hugoniot response than predicted by the EOS models. The data also validate the DFT simulations in the Mbar pressure regime. To date, the experimental results are the highest pressure data points on liquid argon.

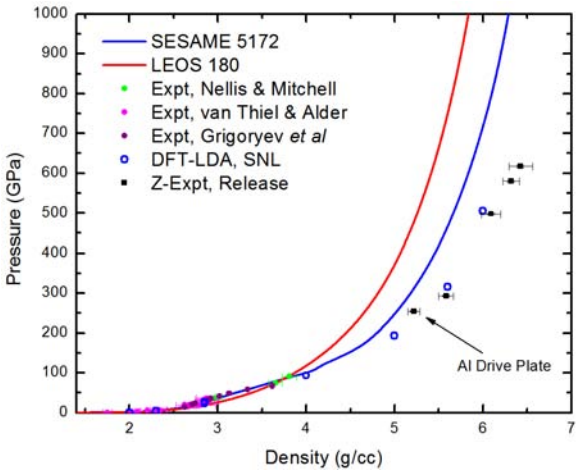

Figure 3.5. $\rho - P$ Hugoniot data for argon from all experiments and DFT simulation results. The existing tabular EOS Hugoniots are also plotted, showing the stiffer response of the models as compared to the data.

Chapter 4

A Wide-Range Equation of State for Argon

The main topic of this paper is to describe the development of a new multi-phase equation of state for argon. A new argon EOS is required due to the poor agreement of prior models with the high pressure Hugoniot data described in the preceding chapters. In addition, development of the new model focused on obtaining a good melting curve as well as a good description of the vapor dome region. The models used for the new EOS are described in Sec. 4.1 with the details of their calibration in Sec. 4.2 and tabulation in Sec. 4.3. Finally, Sec. 4.4 compares the new table with the data and prior models.

4.1 Models

The EOS is based upon the standard separation of the Helmholtz free energy F into ionic and electronic components $F = F_c + F_i + F_e$, where F_c, F_i, and F_e are respectively the cold curve, thermal ionic, and thermal electronic contributions. The models used in the EOS follow closely those used in a prior EOS for xenon [21], with some small modification. In particular, two distinct phases are modeled, a fcc solid and a fluid. Each phase includes a distinct model for each of the three components of the free energy.

4.1.1 Cold curve

The cold curve form in compression expresses the pressure in polynomial form,

$$P_c(Y) = \sum_{i=-1}^{5} b_i Y^i, \tag{4.1}$$

where the $\{b_i\}$ are constants, $\sigma = \rho/\rho_{00}$, and $Y = \sigma^{1/3}$. The free energy is them obtained via

$$F_c = \int_1^{\sigma} P_c(x) x^{-2} dx. \tag{4.2}$$

The seven coefficients of Eq. (4.1) are obtained by requiring that the curve approach the Thomas-Fermi (TF) and Thomas-Fermi-Kirzhnits (TFK) limits for large compressions, that the pressure is zero at equilibrium, that one recovers the desired equilibrium bulk modulus K_0 and pressure derivative of the bulk modulus K_0', and that the third derivative of P_c at $\sigma = 1$ and P_c at $\sigma = 125/64$ match the Vinet form [22]. Explicitly, one has the system of equations,

$$\begin{aligned}
\lim_{Y\to\infty} P_c(Y) &= P_{TF}Y^5 && (4.3)\\
P_c(1) &= 0 && (4.4)\\
K_c(1) = \frac{Y}{3}\frac{dP_c}{dY}(1) &= K_0 && (4.5)\\
\frac{dK_c}{dP}(1) &= K_0' && (4.6)\\
P_c(5) &= P_{TFK} && (4.7)\\
K_c''(1) &= K_V'' && (4.8)\\
P_c(5/4) &= P_V && (4.9)
\end{aligned}$$

where $P_{TF} = 1003.59(\rho_0 Z_{av}/F)^{5/3}$ in units of GPa with Z_{av} and F respectively the average atomic number and formula weight, P_{TFK} is the TFK pressure at 125-fold volume compression, $K_V'' = 3/4K_0(19 + 9K_0'(3K_0' - 2))$ is the value of the left hand side of Eq. (4.8) evaluated for the Vinet form, and $P_V = 15/16K_0\exp(3/10K_0' - 1))$ is the Vinet pressure at $\sigma = 125/64$. The primes on K_c in Eq. (4.8) denote application of the operator $Y\frac{d}{dY}$. Clearly, Eq. (4.3) requires $b_5 = P_{TF}$. The remaining six equations form a linear system which may be solved using standard techniques.

In expansion, $\sigma < 1$, the form of Eq. (4.1) becomes invalid once one strays too far from equilibrium. To ameliorate this fact, a low density polynomial form is matched to Eq. (4.1) at a certain density ρ_{LJ}. The type of form used for F_c in this regime is dependent upon the binding characteristics of the material in question. The following Lennard-Jones based form works well in general for solids,

$$F_c(\rho) = f_1\rho^{f_2} - f_3\rho^{f_{LJ}} + E_B, \tag{4.10}$$

where E_B is the binding energy and f_{LJ} is an adjustable constant [23]. However, this form may encounter problems for some values of f_{LJ}, so the form

$$F_c(x = \rho/\rho_{LJ}) = E_B + x\sum_{i=1}^{6} f_i x^i \tag{4.11}$$

is also used, where f_4, f_5 are adjustable constants. In both cases, the constants f_1, f_2, and f_3 are chosen to ensure that the free energy F_c and its first two derivatives are continuous at $\rho = \rho_{LJ}$. The polynomial form of Eq. (4.11) may have unphysical oscillations for arbitrary choices of f_4 and f_5. Hence an additional parameter f_6 is automatically chosen such that the second derivative

of Eq. (4.11) has no more than one zero for $0 \leq x \leq 1$. This prevents oscillation of the cold curve form while still allowing the physical curvature change between the equilibrium point and infinite expansion.

4.1.2 Thermal ionic terms

The thermal motion of the ions in the solid are modeled using Debye theory. The free energy is given as

$$F_i = \frac{R}{A}\left(\frac{9}{8}\theta + 3T\log\left(1-\exp\left(-\frac{\theta}{T}\right)\right) - TD\left(\frac{\theta}{T}\right)\right), \tag{4.12}$$

where A is the molecular weight, R is the gas constant, and $D(x)$ is the Debye integral. The Debye temperature θ is given by

$$\theta = \theta_r \sigma^{\gamma_\infty} \exp((\gamma_r - \gamma)/\tau_g), \tag{4.13}$$

with

$$\gamma = (\gamma_r - \gamma_\infty)/\sigma^{\tau_g} + \gamma_\infty. \tag{4.14}$$

Here θ_r, γ_r, γ_∞, and τ_g are all constants. In expansion, the Debye model becomes unrealistic due to the inclusion of unrealistic energy states in the integral over the harmonic oscillator frequencies. Therefore, a correction is included that cuts off the integral at the frequency corresponding to the Wigner-Seitz cell radius. The result is that the free energy expression becomes

$$F_i = \frac{R}{A}\left(\frac{9}{8}\theta + F_D\left(\frac{\theta}{T}\right) - F_D\left(\frac{\theta_n}{T}\right)\right), \tag{4.15}$$

where

$$F_D(x) = 3T\log(1-\exp(-x)) - TD(x) \tag{4.16}$$

and

$$\theta_n = 0.2\frac{\theta^2 A M_0}{2\hbar^2}\left(\frac{3AM_0}{4\pi\rho}\right)^{2/3}. \tag{4.17}$$

This cuts off the unrealistic increase in pressure as the density decreases. More details are found in Ref. [23].

To model the thermal motion of the ions in the liquid state, the variational fluid model CRIS was used. This model describes a fluid using a hard sphere system as a reference and has been applied to a variety of systems including noble gases [24] and metals [25]. Through a variational calculation of the size of fluid atoms, a good description is obtained for the compressed fluid. As well, the model exhibits van der Waal's loops and so may be used to describe the vaporization transition. Further detailed descriptions of the model may be found in Refs. [26, 27]. Version 2 of the model as found in revision 2.14 of PANDA [23] was used in the calculations. There are several inputs to the model. The most important is the cold curve for the material of interest. This is input in the form described in Sec. 4.1.1. The other adjustable parameters are E_{fac} and B_{exp}, which are used to modify the melting behavior of the model. Both the cold and thermal ion free energy terms are included in this model.

4.1.3 Thermal electronic terms

For the thermal electronic component, a simplified version of a semi-empirical electronic model developed for metals was used. The basic equations are given below, but a more detailed description may be found in Ref. [28]. The free energy is given by

$$F_e(\sigma,T) = -c_e(\sigma,T)T\log\left(1+\frac{B_e(T)T}{3RZ}\sigma^{-\gamma_e(\sigma,T)}\right) \tag{4.18}$$

where

$$B_e(T) = \frac{2}{T^2}\int_0^T\int_0^{T'}\beta(\tau)d\tau dT', \tag{4.19}$$

$$\beta(T) = \beta_i + \left(\beta_0-\beta_i+\beta_m\frac{T}{T_b}\right)\exp(-T/T_b), \tag{4.20}$$

$$c_e(\sigma,T) = \frac{3R}{2}\left(Z+\frac{\sigma_z\sigma T_z^2(1-Z)}{(\sigma+\sigma_z)(T^2+T_z^2)}\exp(-\tau_i/T)\right), \tag{4.21}$$

$$\tau_i = T_i\exp(-\sigma_i/\sigma), \tag{4.22}$$

and

$$\gamma_e(\sigma,T) = \gamma_i + \left(\gamma_0-\gamma_i+\gamma_m\frac{T}{T_g}\right)\exp\left(-\frac{T}{T_g}\right). \tag{4.23}$$

Here Z is the atomic number, R is the gas constant, and $\sigma = \rho/\rho_r$. The remaining parameters are all adjustable, although they have connections to physical effects. In particular, these equations describe the asymptotic limits of the electron gas as well as ionization and the metal-insulator transition.

4.1.4 High temperature extrapolation

At very high temperatures the fluid model may be unrealistic due to the calibration done for lower temperature data. Thus, an interpolation to TFK theory is included for the fluid model at high temperature. The interpolation uses quintic polynomials for the Helmholtz free energy and pressure to ensure second derivative continuity in the thermodynamic functions. The temperature bounds for interpolation were 10 and 75 eV at densities greater than 1 g/cm^3. Below this density, the bounds were gradually reduced to the minimum interpolation bounds of 1 and 2 eV.

Interpolation between EOS models often results in unphysical oscillations in the thermodynamic functions. To prevent such an occurrence, a constant entropy shift of 0.711 kJ/kg/K, and corresponding linear temperature shift in the free energy, was added to the TFK theory to align the free energy surface more closely with the fluid model. This shift prevented unphysical oscillations in the Hugoniot response in the interpolation region.

4.2 Calibration

The solid model is built from the cold curve models of Eqs. (4.1) and (4.10), the cut off Debye model of Eq. (4.15) and the thermal electronic model of Eq. (4.18). Combined, these models give the solid 26 adjustable parameters. The fluid model uses the cold curve models of Eqs. (4.1) and (4.11), the CRIS model, and the thermal electronic model of Eq. (4.18). With the addition of a constant energy shift parameter E_s this gives the fluid 26 adjustable parameters. To calibrate these parameters, a variety of data was used over a wide range of the phase space as detailed in the following sections.

4.2.1 Compression data

Two measurements of the isothermal compression of argon at room temperature were taken from Refs. [29, 30]. These data sets were then fit to a Vinet cold curve form [22]

$$P(\rho) = a\rho^{2/3}(1-(c/\rho)^{1/3})\exp(b(1-(c/\rho)^{1/3})) \tag{4.24}$$

where a, b, and c are adjustable constants. The results are shown in Fig. 4.1. The fit describes the data well, except for highest compression point. To simplify the calibration procedure, the fit curve was sampled at 11 points between 2.0 and 5.0 g/cm^3 for use as calibration data.

Shock measurements of argon have also been taken from a variety of initial states. Two initial states were chosen for the calibration data set, one in the solid, and one in the liquid. This allows both models to be calibrated to shock data. The solid shock compression data was taken from Ref. [31] and the liquid data from Refs. [18, 32, 33] as well as the Z data from Ch. 3 and DFT calculations from Ch. 2. All these data points are shown in Fig. 4.2. The calculated shock

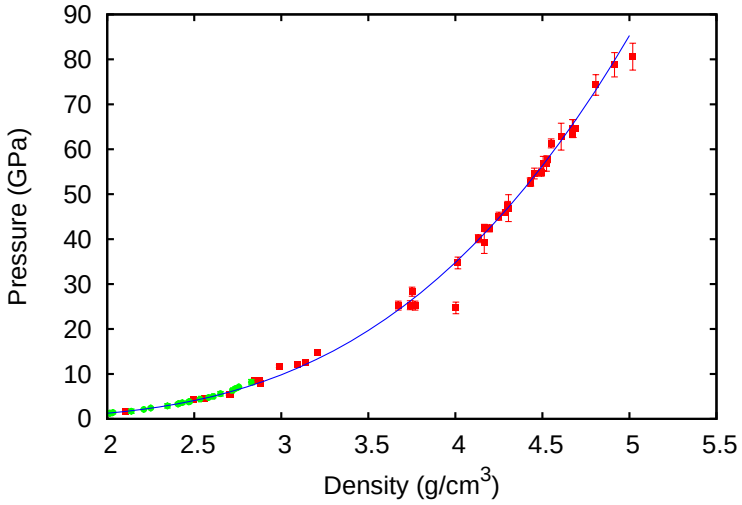

Figure 4.1. Isothermal compression data for argon. Data is shown as green circles [30] and red squares [29]. The blue line is a fit of the two data sets to Eq. (4.24) with $a = 0.163016$ GPa cm^2/g$^{2/3}$, $b = 14.2901$, and $c = 0.959684$ g/cm^3.

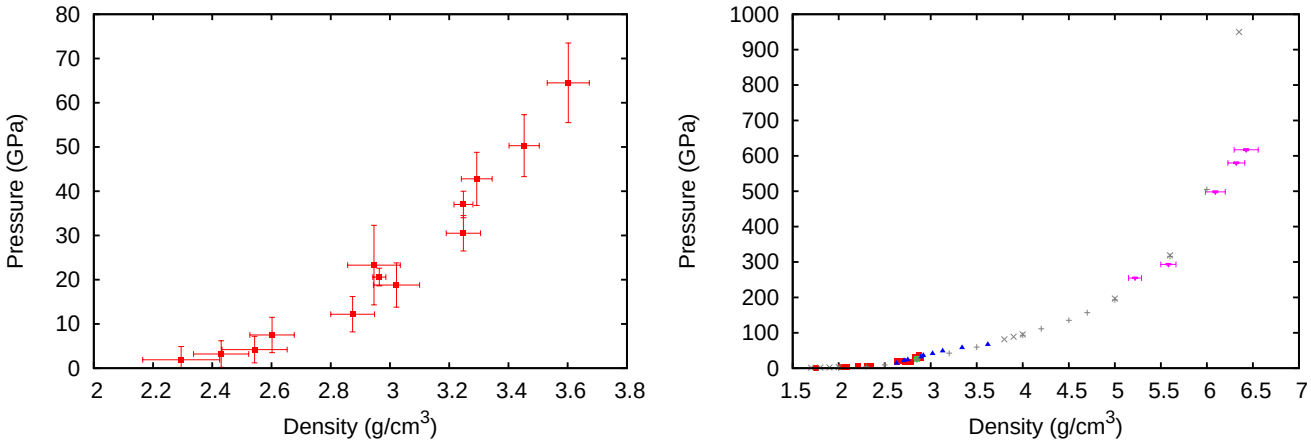

Figure 4.2. Shock compression data for argon from solid and liquid initial states. The solid initial state is at 1.65 g/cm^3 and 75 K with data shown on the left as red squares [31]. The liquid initial state is at 1.4 g/cm^3 and 86 K with data shown on the right as red squares [18], green circles [32], blue triangles [33], magenta inverted triangles for the Z data, and gray exes and pluses for the AM05 and LDA DFT calculations, respectively.

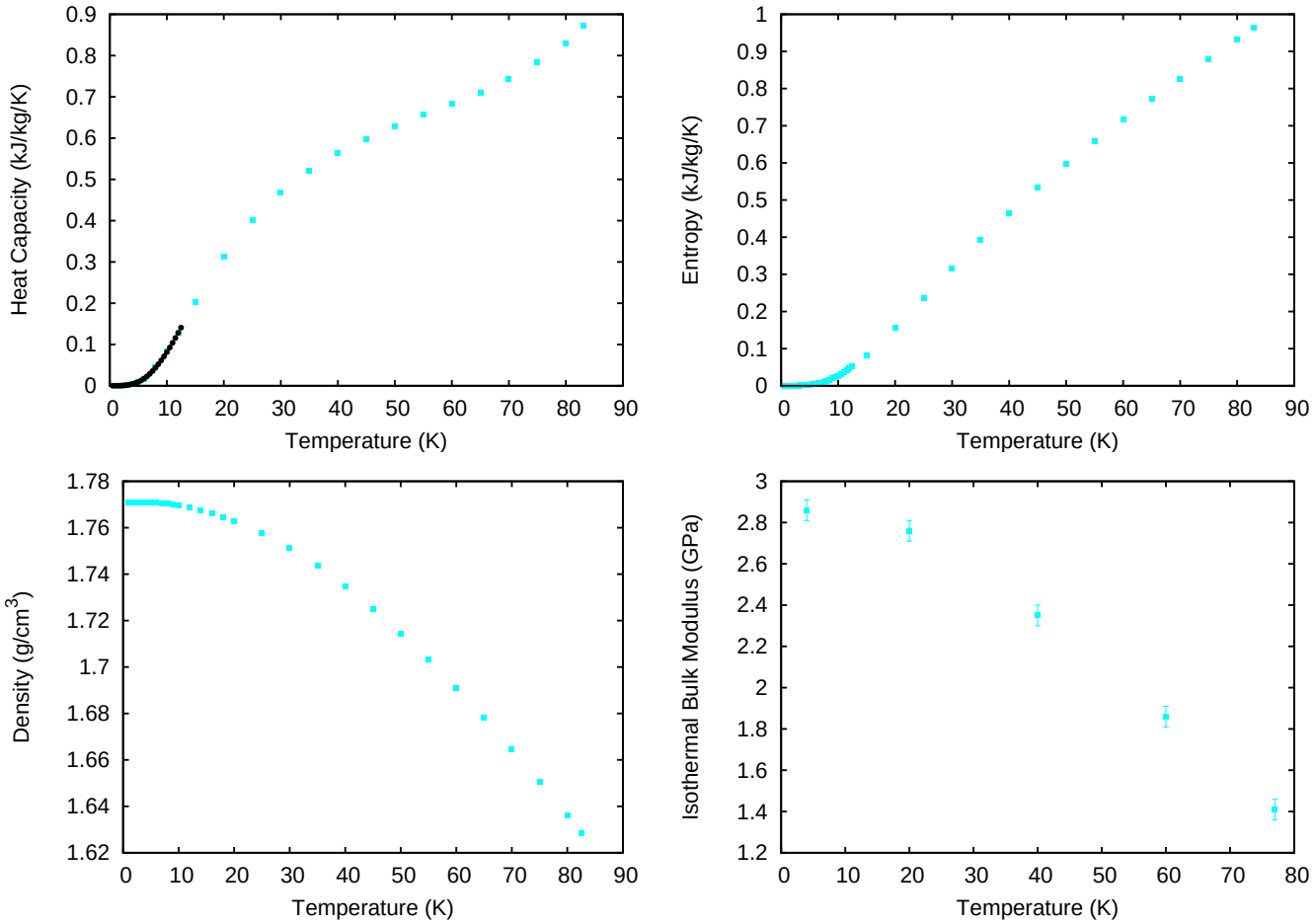

Figure 4.3. Isobaric expansion data for solid argon. Heat capacity data [36, 37] is shown in the top left and the resulting entropy from Eq. (4.25) in the top right. Bottom left plot shows density data [35] and bottom right plot shows isothermal bulk modulus data [34].

temperature data found in Tabs. 2.1-2.2 was also included in the calibration.

4.2.2 Isobaric expansion data

Isobaric expansion data at ambient pressure for solid argon was obtained for the isothermal bulk modulus [34], density [35], and the heat capacity [36, 37], and are shown in Fig. 4.3. For convenience, the heat capacity data was transformed into the entropy and enthalpy using the relations

$$c_P = T\frac{dS}{dT} = \frac{dH}{dT} \tag{4.25}$$

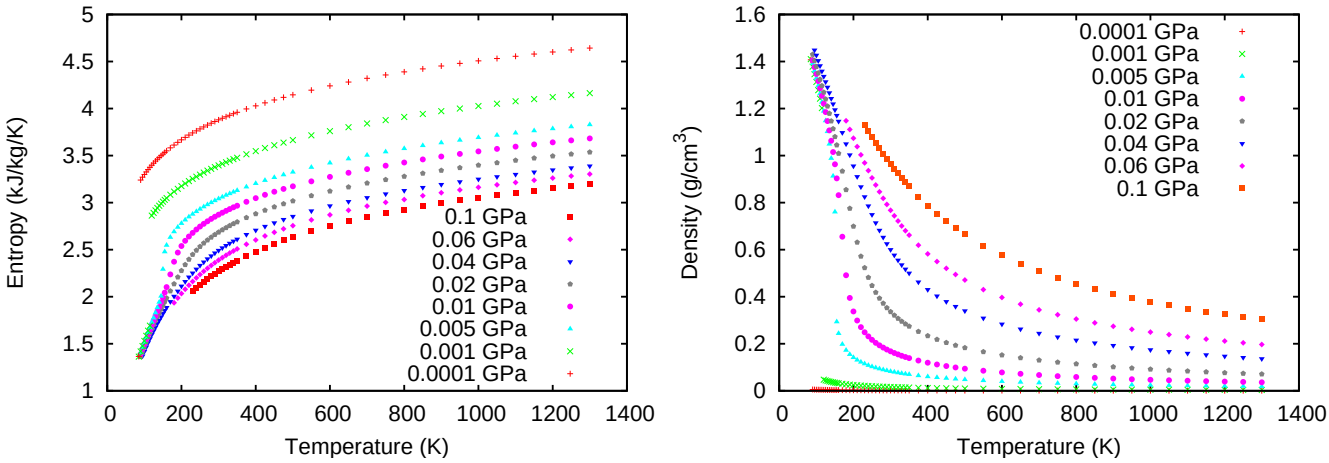

Figure 4.4. Isobaric expansion data for liquid argon. Entropy (left) and density (right) data from Ref. [38] is shown for 8 different pressures.

where constant pressure is assumed. The heat capacity data was numerically integrated using a natural cubic spline interpolant with $\lim_{T\to 0} \frac{c_p}{T^4} = 6.2566 \times 10^{-8}$ MJ/kg/K^4.

Extensive pressure-density-temperature measurements have been made on liquid argon near the liquid-vapor transition up to 1300 K. The data used for calibration was taken from Vargaftik [38] and is shown in Fig. 4.4.

4.2.3 Phase transition data

The vapor dome of argon has been mapped out quite accurately. The critical and triple points are given in Tab. 4.2. The vapor pressure and equilibrium liquid density are shown in Fig. 4.5. Both curves were sampled at 8 temperatures for use in the calibration. The melt curve has also been measured to almost 80 K. The data is shown in Fig. 4.6 along with a fit performed below 50 K to a Simon melt curve using the form

$$T(P) = T_0(P/a+1)^b, \tag{4.26}$$

where a and b are adjustable constants. The ambient melting temperature $T_0 = 83.78$ K was held fixed. The fit melt curve was then sampled up to over 1000 GPa for use in the calibration. This implies ignoring the trend of the DAC data for a much softer melt curve at high pressures. Both recent calculations on xenon [44] and DAC experimental results for tantalum [45] indicate that the deviation of the melt curve from the Simon law at high pressure is much less than measured in some DAC experiments, such as the one reported for argon.

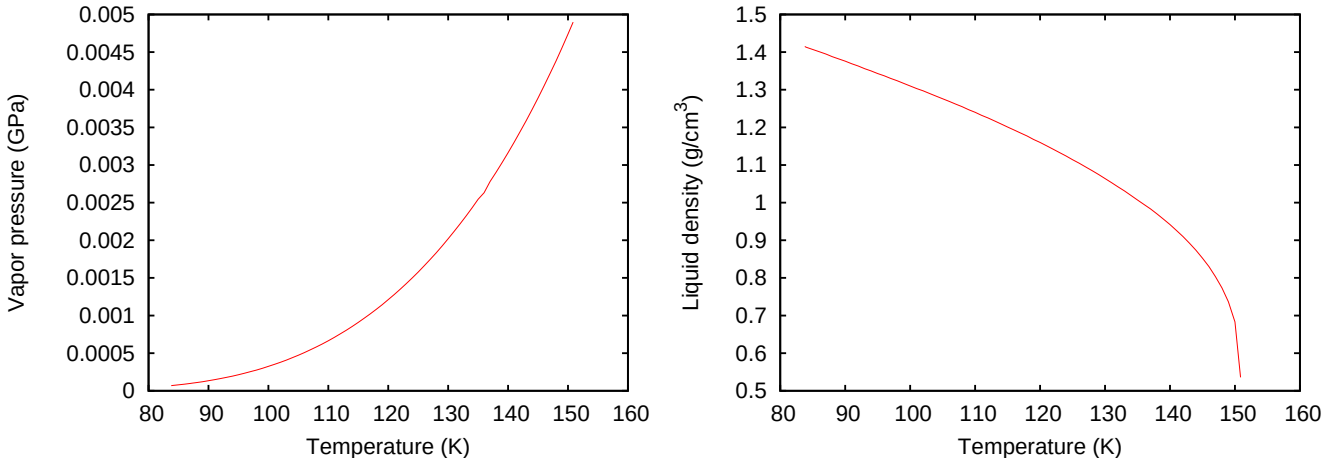

Figure 4.5. Liquid-vapor equilibrium data for argon as taken from Ref. [38]. The left plot displays the vapor pressure and the right plot shows the equilibrium liquid density.

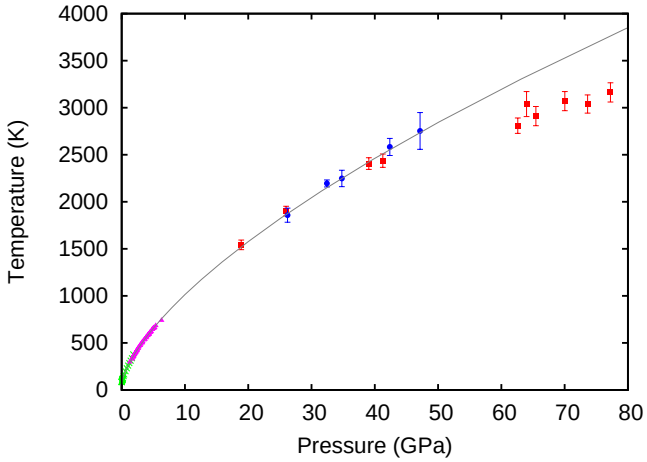

Figure 4.6. Melting curve data for argon. Low pressure experiments [39, 40] are shown as green exes and three DAC experiments are shown as magenta triangles [41], blue circles [42], and red squares [43]. Line shows a fit to the data below 50 GPa using Eq. (4.26) with $a = 0.217736$ GPa and $b = 0.647778$.

4.2.4 Calibration Procedure

Calibration of the model parameters was performed in a series of individual calibrations. First, the solid model was calibrated to all of the solid data. For this fit the electronic model was turned off by fixing the β parameters at zero. Next, the liquid model was fit to all the non-shock liquid data. As with the first solid fit, the electronic model was turned off. Subsequently, the liquid model was calibrated to the Hugoniot, by adjusting only the electronic model parameters, holding the others fixed at the prior values. Last, the high pressure melt curve was fit by varying the solid model electronic term keeping all other parameters fixed except the energy shift for the liquid model, which affects the melt boundary location without changing agreement with the other liquid data. The final parameter set for the models is shown in Tab. 4.1.

4.3 Tabulation

The model described above was tabulated in SESAME format [46] and given the number 5173. Only a 301 table, the total equation of state, is included. The pressure, internal energy, and Helmholtz free energy are included in the tabulation. The temperature grid was chosen such that the logarithm of the pressure would be equally spaced at the critical density. The spacing was chosen so that 11 temperatures were tabulated in the vapor dome. Maxwell constructions were created inside all phase coexistence regions. Below the triple point the isotherm pressure spacing was increased to avoid an unnecessary large table. There are 4 isotherms below 20 K which contain a tension region without solid-gas coexistence.

Once the temperature grid was fixed, the density grid was chosen. Grid points were placed at the edge of every Maxwell construction. Also, points were added to ensure that inside every Maxwell construction there was at least one tabulation point. Finally, additional density points were added to provide a more uniform density grid, to aid in reducing interpolation errors.

The final table contains 159 density and 71 temperature points, spanning the ranges 1×10^{-13} to 100 g/cm^3 in density and 1×10^{-6} to 2.23×10^8 K in temperature. The table reference point was chosen to be the ambient gas density. The first section of the table is shown in Appx. A.

4.4 Comparisons

In this section, two other SESAME tables for argon are compared with the new 5173. First, is table 5172 from the LANL database. It contains Maxwell constructions and a smeared out melting region. A complicated set of models was used to create the 5172 table [47]. The second table, denoted herein as 180L, was created using the LLNL LEOS tools. It contains van der Waal loops in the liquid-vapor region and does not model melt.

The models are compared with the isothermal compression data for solid argon in Fig. 4.7.

Table 4.1. Parameters and their values for model 5173.

Solid model parameters			
ρ_{00}	1.8283 g/cm^3	T_i	900.86 K
K_0	3.2718 GPa	T_g	123049. K
K_0'	7.4505	σ_z	0.84331
ρ_{LJ}	1.7569 g/cm^3	σ_e	1.0
f_{LJ}	2.3938	σ_d	9.99E+99
E_B	0.20380 MJ/kg	σ_i	0.3
θ_r	118.88 K	β_i	1.9662E-07 MJ/kg/K^2
ρ_r	2.0038 g/cm^3	β_0	2.7447E-07 MJ/kg/K^2
γ_r	2.5200	β_m	1.1047E-07 MJ/kg/K^2
γ_∞	1.3150	γ_i	0.51815
γ_τ	1.0	γ_0	0.13481
T_b	2522.3 K	γ_m	0.77737
T_z	199000. K	ρ_{re}	3.0829 g/cm^3
Fluid model parameters			
ρ_{00}	1.83 g/cm^3	T_z	200000. K
K_0	3.316 GPa	T_i	5000. K
K_0'	7.67	T_g	500000. K
ρ_{LJ}	1.8117 g/cm^3	σ_z	0.8
f_4	0.74932 MJ/kg	σ_e	2.3
f_5	-0.28448 MJ/kg	σ_d	9.0
f_6	1.0E-8 MJ/kg	σ_i	0.3
E_B	0.17032 MJ/kg	β_i	4.75E-08 MJ/kg/K^2
B_{exp}	6.2 g$^{1/3}$/cm	β_0	1.8E-17 MJ/kg/K^2
E_{fac}	3.4448 MJ/kg	β_m	0.0 MJ/kg/K^2
E_s	0.040578 MJ/kg	γ_i	0.66667
ρ_r	1.83 g/cm^3	γ_0	0.15
T_b	10000. K	γ_m	0.0

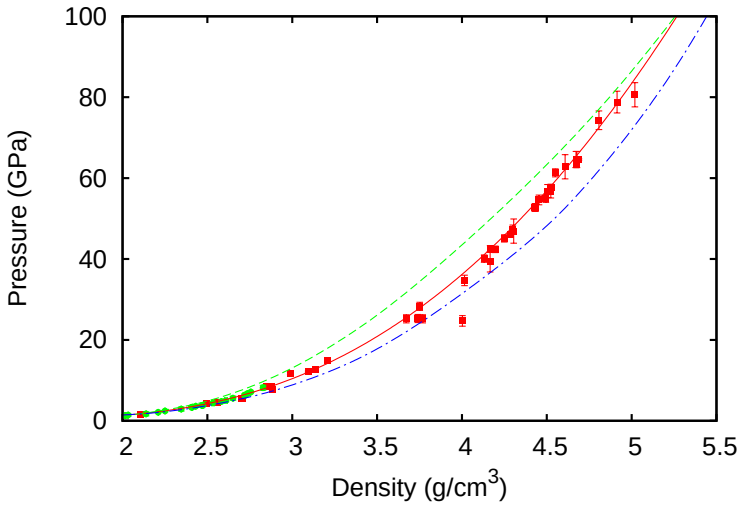

Figure 4.7. Isothermal compression results for argon. Data is as in Fig. 4.1. Results are shown for table 5173 (solid red line), 5172 (dash-dot blue line), and 180L (dashed green line).

Both 5172 and 180L do not agree well with the data above around 3 g/cm^3, lying below and above the experimental results, respectively. On the other hand 5173 is in good agreement. In Fig. 4.8 the models are compared with the solid isobaric expansion data. Entropy was not tabulated except for 5173, which agrees well with the data. Instead of comparing with the heat capacity, the enthalpy is shown in Fig. 4.8 for the various models. Again 5173 agrees well with the data, and the jump in enthalpy at melt is seen near the highest temperature data point. Here 180L gets the general slope of the curve correct at the higher temperatures, but is significantly shifted from the data, indicating poor description of the low temperature behavior. The 5172 model does not tabulate temperatures below 116 K and so does not describe the solid data shown in Fig. 4.8 except through extrapolation. This results in extremely poor agreement, as seen in the enthalpy plot. For the solid density and bulk modulus, 180L displayed similar behavior, being close to, but not in good agreement with the data. The 5173 model is very close to the density results but displays a stair step effect. This arises due to the tabulation of Maxwell constructions in the sublimation region. At ambient pressure, interpolation patches cover states both in the Maxwell constructions and in the solid phase. Interpolation schemes based upon a rectangular grid do not resolve this region well. The effect is seen more predominantly in derivatives, such as the bulk modulus. The interpolated bulk modulus for 5173 is clearly in very poor agreement with the data due to this fact. However, Fig. 4.8 also displays the 5173 model bulk modulus derived directly from the model, which agrees well with the data.

For tabulation convenience, sublimation Maxwell constructions were included in the 5173 table. Even with mesh refinement, the issues with interpolation would remain in this region. Due to the low temperature, the solid is typically not accessed at ambient pressure. Thus these interpolation issues should not significantly impact simulations. If this region was important, one might want to revisit the tabulation choice to include tension instead of the Maxwell constructions.

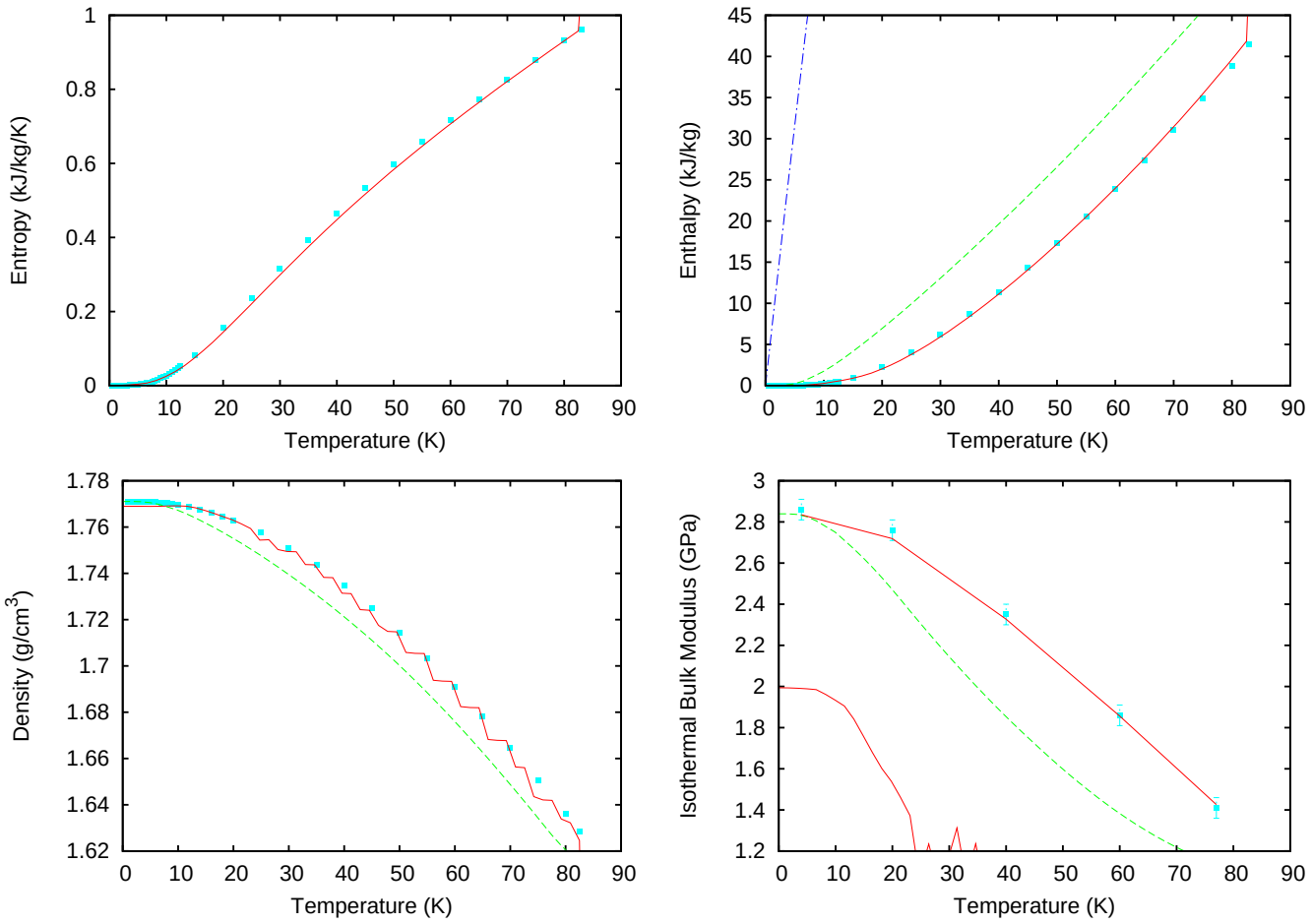

Figure 4.8. Isobaric expansion results for solid argon. Entropy and enthalpy are shown in the top left and right plots respectively, with density and isothermal bulk modulus on the bottom left and right plots respectively. Data is as shown in Fig. 4.3 and lines are as in Fig. 4.7.

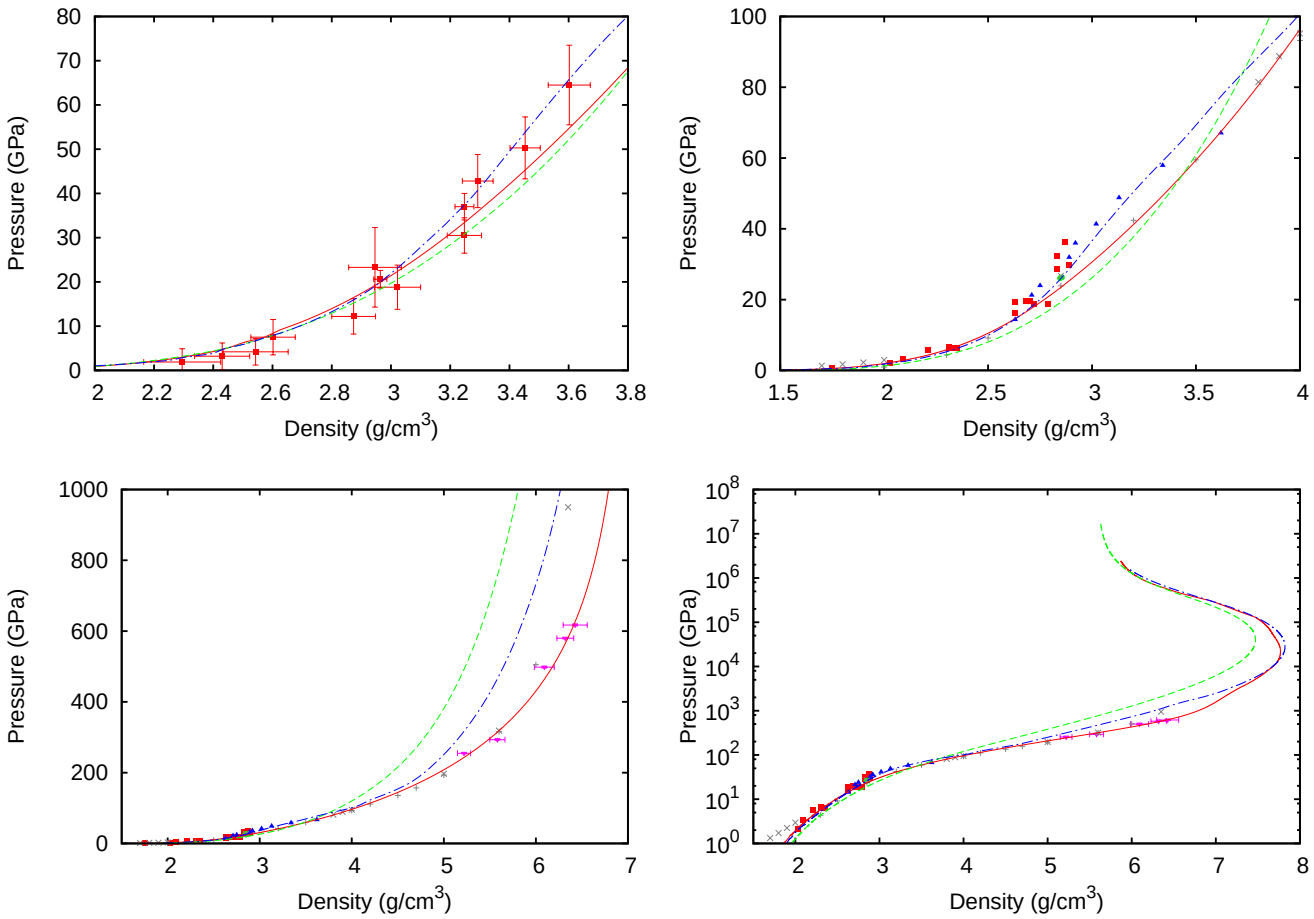

Figure 4.9. Shock compression results for argon from solid and liquid initial states. The solid results are shown on the top left. The top right, and bottom left and right plots show the liquid results at successively higher pressures. Data is as in Fig. 4.2 and lines as in Fig. 4.7.

The shock compressed solid results are shown in the top left of Fig. 4.9. Here all three EOS model agree with the data, due to the large uncertainties, but arguably the 5172 model agrees best. There is some question as to whether the stiffer response is appropriate. Examining the low pressure liquid shock response in the top right of Fig. 4.9 shows a similar result to the solid. In particular 5172 has a much stiffer response below 3.5 g/cm^3 that corresponds well with the experimental data. However, the DFT calculations do not indicate the stiffer response indicated by the experimental data. At these two-fold compressions, the DFT results are expected to be accurate, calling into question what process is responsible for the difference with the experimental data. With this in mind the 5173 model was developed to agree with the low pressure (< 10 GPa) experiments, the high pressure (> 60 GPa) experiments, and the DFT calculations at all pressures.

Examining the bottom plots in Fig. 4.9 shows the high and extreme pressure Hugoniot response

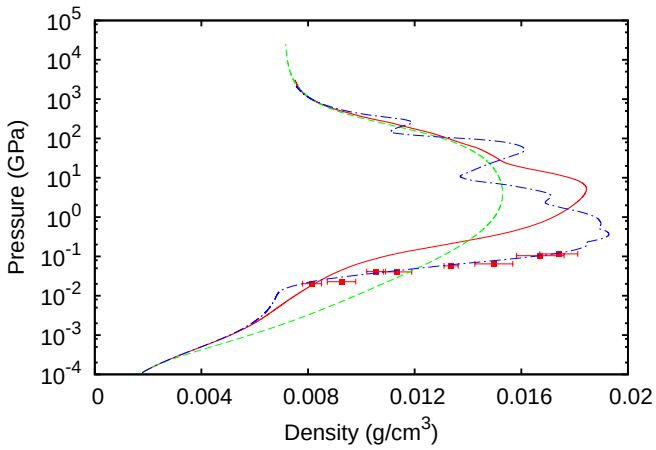

Figure 4.10. Gas shock compression results for argon with initial state at ambient conditions. Data is from Ref. [48], scaled to 1 bar initial pressure, and lines are as in Fig. 4.7.

for the models. Both 5172 and 180L do not agree with the DFT and experimental data in this regime. Indeed, this was the impetus for creating the new 5173 model, which can bee seen to agree well with both the DFT-MD computations as well as the high pressure Z experiments. At extreme pressures the models all use the average atom Thomas-Fermi theories. Both 5172 and 5173 include gradient corrections and predict a higher maximum compression, while 180L predicts a smaller maximum compression.

The shock response from an initial gaseous state has also been measured and is shown in Fig. 4.10. Here the 5172 model is in good agreement due to its incorporation of ionization equilibrium theory. In particular, it describes very well the first ionization. Experiments are not available to test the oscillations predicted at high pressures. Both 180L and 5173 average out the oscillations due to ionization, although 5173 qualitatively provides a better approximation. Due to the choice of models in 5173 it was not possible to simultaneously get good agreement with the liquid expansion data and the gas shock results. The decision was made to allow some disagreement in the gas Hugoniot to provide better agreement at low temperatures near the vapor dome.

To the authors' knowledge, the shock temperature from the liquid state has not been measured experimentally. However, the DFT calculations of Ch. 2 provide a good estimate for those temperatures. The results are compared in Fig. 4.11. The 5173 model agrees well with the DFT data. The results of 180L also lie quite close, although at slightly higher temperatures. Interestingly, 5172 predicts a much higher shock temperature than the data, despite it being closer to the correct pressure response than 180L.

Low temperature fluid expansion results are shown in Fig. 4.12. In the top left the entropy data is shown and 5173 agrees well with the data except at the lowest pressure and highest temperature. The other tables do not include entropy data. However, the enthalpy may be calculated and this shows similar trends to what one sees in entropy space. Again, 5173 agrees well with the data

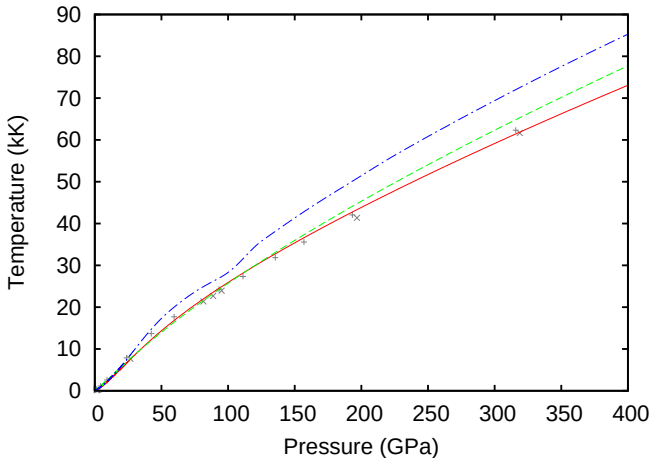

Figure 4.11. Liquid shock compression temperature results for argon. The liquid initial state is the same as in Fig. 4.9. The DFT calculation data is as in Fig. 4.2 and lines are as in Fig. 4.7.

Table 4.2. Critical and triple points for argon. The experimental values are given along with the three EOS tables under comparison. Subscripts c and t respectively denote the critical and triple point. The listed triple point density is for the liquid. All experimental values have estimated errors of less than one percent.

	T_c (K)	ρ_c (g/cm^3)	P_c (MPa)	T_t (K)	ρ_t (g/cm^3)	P_t (kPa)
Expt.	150.86	0.5356	4.898	83.78	1.415	68.75
5172	174.96	0.425	6.785	—	—	—
180L	174.76	0.8	6.786	—	—	—
5173	151.31	0.4537	5.122	83.49	1.418	86.60

except for the same low pressure region seen in the entropy. Also, 5172 is in good agreement with data at all pressures and high temperatures, At low temperatures it does not agree as well with data near the critical point, as will be seen again below. The 180L model deviates strongly from the enthalpy data as the temperature increases. The deviations at high temperature are reflected in the deviations from the gas shock results in Fig. 4.10.

The liquid density results in Fig. 4.12 show a similar trend to the enthalpy results. Both 5172 and 5173 agree well with the data, although at low temperatures they straddle the experimental results. On the other hand 180L is a poor approximation to the data at low temperatures.

In examining the phase behavior of argon, the liquid-vapor curve is shown first in Fig. 4.13. The curve stretches from the triple point at low temperature to the critical point at high temperature. The values for these points in each model is shown in Tab. 4.2. One can see that the 5173 model

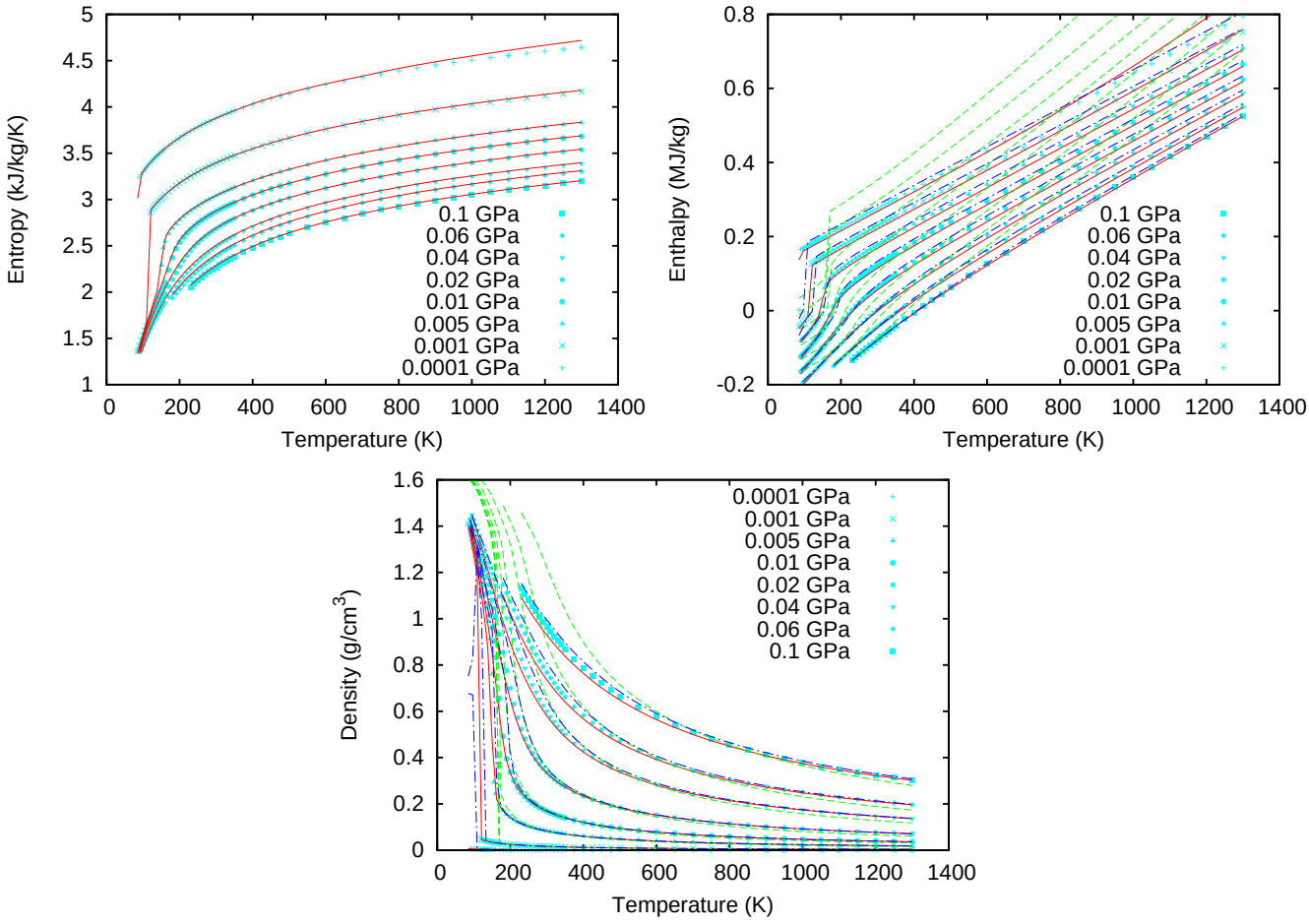

Figure 4.12. Isobaric expansion results for liquid argon. Entropy (top left), enthalpy (top right), and density (bottom) are shown with data as in Fig. 4.4 with curves as in Fig. 4.7. Enthalpy results are shifted to prevent overlap of the data.

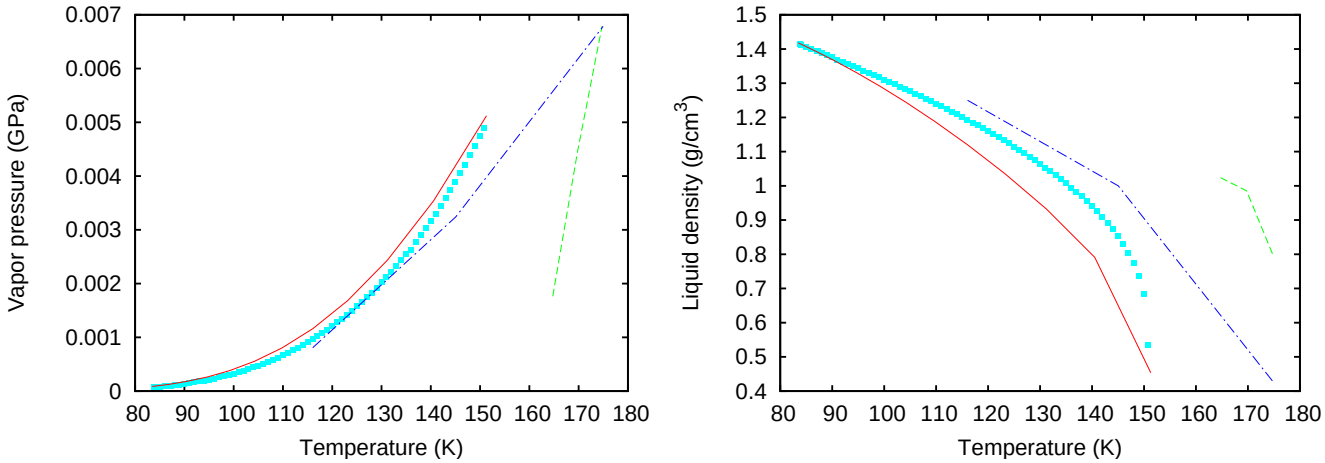

Figure 4.13. Liquid-vapor equilibrium results for argon. Data is as in Fig. 4.5 but shown as cyan squares. Lines are as in Fig. 4.7. The left plot displays the vapor pressure and the right plot shows the equilibrium liquid density. For both 5172 and 180L only three points are shown, connected by straight lines as guides to the eye. In both cases, the estimated critical point is include. For 5172 the two tabulated Maxwell constructions give the other two points. For 180L, Maxwell constructions were calculated at two temperatures 5 and 10 K below the critical point.

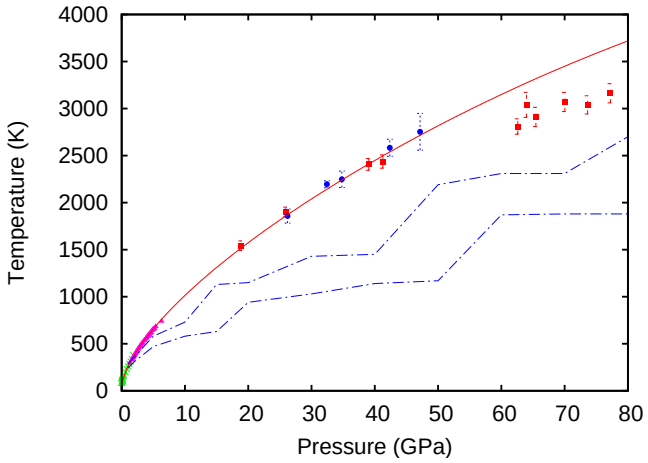

Figure 4.14. Melting curve results for argon. Data is as in Fig. 4.6 and lines as in Fig. 4.7. The two lines for 5172 give the boundaries of the melt region.

agrees well with the vapor pressure data. However, it does not agree well over the complete range of the saturated liquid density. This is a known deficiency of fluid models. In particular, typically only two of the critical pressure, density, and temperature may be matched. For 5173 the decision was made to match the pressure and temperature at the critical point and then density at the triple point, but allow the critical density to vary from the experimental measurements. This allows a good description of the initial liquid Hugoniot state, in coordination with a good melt curve, while still having a reasonable vapor dome, although it is shifted to smaller densities.

The 5172 model does worse than 5173 in describing the vaporization behavior of argon. None of the critical values are close to the experimental values, which leads the resulting vapor curves in Fig. 4.13 to be in poor agreement. The 180L model is even poorer, with the vapor pressure and liquid saturation density not even lying close to the data.

The melt curve results are shown in Fig. 4.14. By construction the 5173 model agrees very well with the data up to 50 GPa, above which it was specifically chosen to lie at higher temperatures, as discussed in Sec. 4.2. The 180L model does not include a melt transition. The melt transition in 5172 is significantly smeared out, and was detected by computing isobars and looking for an apparent jump in enthalpy. The general trend is for 5172 to significant underestimate the melt temperature above 5 GPa.

Chapter 5

Summary and discussion

In this report, we have presented results from DFT based QMD simulations, high-precision shock experiments up to 600 GPa/ 6 Mbar on Sandia's Z-machine, and developed a new tabular equation of state for argon. Previously, the behavior of argon was not known experimentally beyond approximately 100 GPa under shock conditions and existing equation of state models differ significantly. This report thus increases by a factor of 6 the regime in pressure where the behavior of argon is known.

Besides providing a new tabular EOS, high-fidelity results from simulations, and experimental data, the work illustrates how difficult it is to extrapolate equation of state (EOS) models beyond pressures where experimental data, or results from high-fidelity simulations, are available.

Future work in this area will focus on measuring temperature and developing methods for off-Hugoniot measurements. Temperature measurements are needed to further constrain the equation of state on the Hugoniot and off-Hugoniot measurements cover the significant area in the phase-diagram between the cold curve and the Hugoniot. When put together, the new measurements will give an even better understanding of the behavior of argon under shock compression.

References

[1] S. Root *et al.*, Phys. Rev. Lett. **105**, 085501 (2010).

[2] M. Desjarlais, Phys. Rev. B **68**, 064204 (2003).

[3] M. D. Knudson *et al.*, Phys. Rev. Lett. **87**, 225501 (2001).

[4] M. D. Knudson, M. P. Desjarlais, and D. H. Dolan, Science **322**, 1822 (2008).

[5] P. Hohenberg and W. Kohn, Phys. Rev. **136**, B864 (1964).

[6] W. Kohn and L. J. Sham, Phys. Rev. **140**, A1133 (1965).

[7] N. Mermin, Phys. Rev. **137**, A1441 (1965).

[8] M. Allen and D. Tildesley, *Computer Simulations of Liquids* (Oxford Science Publications, 1987).

[9] M. E. Savage *et al.*, in *2007 IEEE Pulsed Power Conference* (2007), vol. 1-4, p. 979.

[10] D. L. Hanson *et al.*, in *Shock Compression of Condensed Matter - 1999* (2000), vol. 505, p. 1175.

[11] A. C. Sinnock and B. L. Smith, Phys. Rev. **181**, 1297 (1969).

[12] A. C. Sinnock, J. Phys. C: Solid St. Phys. **13**, 2375 (1980).

[13] L. M. Barker and R. E. Hollenbach, J. Appl. Phys. **43**, 4669 (1972).

[14] M. D. Knudson and M. P. Desjarlais, Phys. Rev. Lett **103**, 225501 (2009).

[15] M. D. Knudson and M. P. Desjarlais, quartz release data and model.

[16] M. D. Knudson, R. W. Lemke, D. B. Hayes, C. A. Hall, C. Deeney, and J. R. Asay, J. Appl. Phys. **94**, 4420 (2003).

[17] S. Root *et al.*, krypton Hugoniot.

[18] M. Van Thiel and B. J. Alder, J. Chem. Phys. **44**, 1056 (1966).

[19] W. J. Nellis and A. C. Mitchell, J. Chem. Phys. **73**, 6137 (1980).

[20] F. B. Grigoryev, S. B. Kormer, O. L. Mikhailova, M. A. Mochalov, and V. D. Urlin, Journal of Experimental and Theoretical Physics **88**, 1271 (1985).

[21] J. H. Carpenter, D. G. Flicker, S. Root, R. J. Magyar, D. L. Hanson, and T. R. Mattsson, EPJ Web of Conferences **10**, 00018 (2010).

[22] P. Vinet, J. H. Rose, J. Ferrante, and J. R. Smith, J. Phys.: Condens. Matter **1**, 1941 (1989).

[23] G. I. Kerley, Tech. Rep. SAND88-2291, Sandia National Laboratories (1991).

[24] G. I. Kerley, Tech. Rep. LA-4760, Los Alamos Scientific Laboratory (1971).

[25] G. I. Kerley, Int. J. Impact Engng. **5**, 441 (1987).

[26] G. I. Kerley, J. Chem. Phys. **73**, 469 (1980).

[27] G. I. Kerley, J. Chem. Phys. **73**, 478 (1980).

[28] A. V. Bushman *et al.*, *Intense dynamic loading of condensed matter* (Taylor & Francis, Washington DC, 1993).

[29] M. Ross, H. K. Mao, P. M. Bell, and J. A. Xu, J. Chem. Phys. **85**, 1028 (1986).

[30] L. W. Finger, R. M. Hazen, G. Zou, H. K. Mao, and P. M. Bell, Appl. Phys. Lett. **39**, 892 (1981).

[31] R. D. Dick and R. H. Warnes, J. Chem. Phys. **53**, 1648 (1970).

[32] S. P. Marsh, ed., *LASL Shock Hugoniot Data* (University of California Press, Berkeley, 1980).

[33] R. F. Trunin, L. F. Gudarenko, M. V. Zhernokletov, and G. V. Simakov, *Experimental Data on Shock Compression and Adiabatic Expansion of Condensed Matter* (RFNC-VNIIEF, Sarov, 2001).

[34] M. S. Anderson and C. A. Swenson, J. Phys. Chem. Solids **36**, 145 (1975).

[35] Y. S. Touloukian, R. K. Kirby, R. E. Taylor, and T. Y. R. Lee, *Thermal Expansion Nonmetallic Solids* (IFI/Plenum, New York, 1977), p. 2.

[36] L. Finegold and N. E. Phillips, Phys. Rev. **177**, 1383 (1969).

[37] P. Flubacher, A. J. Leadbetter, and J. A. Morrison, Proc. Phys. Soc. **78**, 1449 (1961).

[38] N. B. Vargaftik, *Tables on the Thermophysical Properties of Liquids and Gases in Normal and Dissociated States* (Hemisphere Publishing Corporation, Washington, D.C., 1975), p. 543.

[39] A. Michels and C. Prins, Physica **28**, 101 (1962).

[40] P. H. Lahr and W. G. Eversold, J. Chem. Engng. Data **7**, 42 (1962).

[41] F. Datchi, P. Loubeyre, and R. LeToullec, Phys. Rev. B **61**, 6535 (2000).

[42] A. P. Jephcoat and S. P. Besedin, Phil. Trans. R. Soc. Lond. A **354**, 1333 (1996).

[43] R. Boehler, M. Ross, P. Söderlind, and D. B. Boercker, Phys. Rev. Lett. **86**, 5731 (2001).

[44] L. Schulenburger and T. R. Mattsson, "Diffusion Monte Carlo calculations of Xenon and Krypton at High Pressures," Shock Compression of Condensed Matter 2011.

[45] A. Dewaele *et al.*, Phys. Rev. Lett. **104**, 255701 (2010).

[46] Tech. Rep. LA-UR-92-3407, Los Alamos National Laboratory (1992).

[47] J. Wolford and K. Long, "A New Theoretical EOS for Argon," in H-Division Quarterly Report UCID-18574-81-3, Lawrence Livermore National Laboratory, Livermore CA 94550 (1981).

[48] R. H. Christian and F. L. Yarger, J. Chem. Phys. **23**, 2042 (1955).

[49] URL `http://t1web.lanl.gov/newweb_dir/t1sesame.html`.

Appendix A

SESAME 5173

The SESAME 5173 table is available from the LANL database [49]. In total it contains 6,832 lines of text and so is not included in this document. However, for reference the first 89 lines are shown below, which include the table up to the next to maximum pressure at the lowest temperature.

```
 0  5173   101   160   r    82212    82212   1                                  0
material. argon(z= 18.00 a=39.948)/source. J. H. Carpenter (jhcarpe@sandia.gov)/
date. Aug 22 2012/refs. SAND2012-XXXX/comp. Ar/codes. /
 1  5173   102   320   r    82212    82212   1                                  1
 Debye solid model with CRIS liquid model. Electronic term uses generalized meta
l form interpolated to TFK theory at high temperatures. Equilibrium 301 table ha
s Maxwell constructions along all phase boundaries except for a very small tensi
on region below 20 K. Pressure, internal energy, and entropy are tabulated.
 1  5173   201     5   r    82212    82212   1                                  1
 1.80000000E+01 3.99480000E+01 1.78000000E-03 1.10025000E-04 0.00000000E+0011111
 1  5173   301 34099   r    82212    82212   1                                  1
 1.59000000E+02 7.10000000E+01 1.00000000E-13 4.32191504E-13 2.00000000E-1211111
 7.93576327E-12 3.00000000E-11 1.16029689E-10 5.00000000E-10 1.77479847E-0911111
 5.60000000E-09 1.64894003E-08 5.60000000E-08 1.43169266E-07 3.60000000E-0711111
 8.46645183E-07 2.20000000E-06 4.94121993E-06 2.00960301E-05 8.10970314E-0511111
 2.29646882E-04 6.47365357E-04 1.28939784E-03 2.56762606E-03 3.62572745E-0311111
 5.12584284E-03 7.21362014E-03 1.01736986E-02 1.42117236E-02 2.00450029E-0211111
 2.83701448E-02 4.03674042E-02 5.79167247E-02 8.42213725E-02 1.25430821E-0111111
 1.96797781E-01 2.50000000E-01 3.10000000E-01 3.80000000E-01 4.53677000E-0111111
 5.50000000E-01 6.60000000E-01 7.90818638E-01 9.32044002E-01 1.03679230E+0011111
 1.12001362E+00 1.18793962E+00 1.24416176E+00 1.29114122E+00 1.33070699E+0011111
 1.36505936E+00 1.39342864E+00 1.41790830E+00 1.43271170E+00 1.44739502E+0011111
 1.46271037E+00 1.47801285E+00 1.49388181E+00 1.50000000E+00 1.51052945E+0011111
 1.52818789E+00 1.54712092E+00 1.56763740E+00 1.59010388E+00 1.61495564E+0011111
 1.62451050E+00 1.62940863E+00 1.63358099E+00 1.63494199E+00 1.64141747E+0011111
 1.64174129E+00 1.64604036E+00 1.64858026E+00 1.65581781E+00 1.65670238E+0011111
 1.66593320E+00 1.66752246E+00 1.67645603E+00 1.68178940E+00 1.68849658E+0011111
 1.68911387E+00 1.69316742E+00 1.70233371E+00 1.70516990E+00 1.71459711E+0011111
 1.71831107E+00 1.72384783E+00 1.73110500E+00 1.73684728E+00 1.73799571E+0011111
 1.74358899E+00 1.74831287E+00 1.74926364E+00 1.75426828E+00 1.75866579E+0011111
 1.76109811E+00 1.76200000E+00 1.76300000E+00 1.79646582E+00 1.82878440E+0011111
 1.83000000E+00 1.84779609E+00 1.88000000E+00 1.92113456E+00 1.93648782E+0011111
 1.98000000E+00 2.02326849E+00 2.07791714E+00 2.12000000E+00 2.16096858E+0011111
 2.22000000E+00 2.26043001E+00 2.30000000E+00 2.34106886E+00 2.42000000E+0011111
 2.49355945E+00 2.53000000E+00 2.57200785E+00 2.65000000E+00 2.72000000E+0011111
 2.79072381E+00 2.83000000E+00 2.86590014E+00 3.00000000E+00 3.17082304E+0011111
```

```
 3.20000000E+00 3.24020312E+00 3.45000000E+00 3.66146937E+00 3.69000000E+0011111
 3.72085679E+00 4.00000000E+00 4.32185799E+00 4.35000000E+00 4.36668254E+0011111
 4.90000000E+00 5.43951740E+00 5.46000000E+00 5.48157693E+00 6.60000000E+0011111
 7.75591614E+00 7.80000000E+00 7.84313346E+00 9.80000000E+00 1.19467790E+0111111
 1.20300000E+01 1.21213556E+01 1.58000000E+01 1.93518928E+01 1.95000000E+0111111
 1.96465361E+01 2.65000000E+01 3.33425122E+01 3.35600000E+01 3.37608345E+0111111
 5.00000000E+01 6.60067786E+01 6.62000000E+01 6.64731944E+01 8.50000000E+0111111
 1.00000000E+02 1.00000046E-06 6.03440908E+00 1.20688182E+01 1.81032272E+0111111
 2.41376363E+01 2.77237873E+01 3.13122714E+01 3.49863468E+01 3.83258329E+0111111
 4.21584705E+01 4.59352900E+01 5.04433492E+01 5.47468550E+01 5.98693736E+0111111
 6.44054957E+01 6.97060540E+01 7.37643526E+01 7.83297077E+01 8.08296420E+0111111
 8.34898582E+01 8.68597118E+01 9.05356021E+01 9.47097814E+01 9.92103939E+0111111
 1.04206262E+02 1.09784389E+02 1.16052649E+02 1.23145846E+02 1.31233757E+0211111
 1.40530631E+02 1.51305339E+02 1.65442095E+02 1.86128141E+02 2.16483929E+0211111
 2.61174504E+02 3.27196547E+02 4.25061817E+02 5.70565220E+02 7.87397524E+0211111
 1.11095956E+03 1.59384405E+03 2.31346990E+03 3.38202120E+03 4.95757591E+0311111
 7.25233726E+03 1.05304550E+04 1.50909137E+04 2.12412801E+04 2.92509385E+0411111
 3.92270506E+04 5.09689236E+04 6.40892789E+04 7.83687493E+04 9.39245889E+0411111
 1.11164200E+05 1.30740221E+05 1.53586987E+05 1.81052555E+05 2.15148379E+0511111
 2.58993150E+05 3.17574747E+05 3.99017551E+05 6.90447901E+05 1.33461266E+0611111
 2.70105692E+06 5.55820224E+06 1.15671945E+07 2.41951467E+07 5.07183414E+0711111
 1.06416867E+08 2.23376531E+08 3.16000000E-17 3.16000000E-17 3.16000000E-1711111
 3.16000000E-17 3.16000000E-17 3.16000000E-17 3.16000000E-17 3.16000000E-1711111
 3.16000000E-17 3.16000000E-17 3.16000000E-17 3.16000000E-17 3.16000000E-1711111
 3.16000000E-17 3.16000000E-17 3.16000000E-17 3.16000000E-17 3.16000000E-1711111
 3.16000000E-17 3.16000000E-17 3.16000000E-17 3.16000000E-17 3.16000000E-1711111
 3.16000000E-17 3.16000000E-17 3.16000000E-17 3.16000000E-17 3.16000000E-1711111
 3.16000000E-17 3.16000000E-17 3.16000000E-17 3.16000000E-17 3.16000000E-1711111
 3.16000000E-17 3.16000000E-17 3.16000000E-17 3.16000000E-17 3.16000000E-1711111
 3.16000000E-17 3.16000000E-17 3.16000000E-17 3.16000000E-17 3.16000000E-1711111
 3.16000000E-17 3.16000000E-17 3.16000000E-17 3.16000000E-17 3.16000000E-1711111
 3.16000000E-17 3.16000000E-17 3.16000000E-17 3.16000000E-17-4.39656260E-0411111
-1.17698246E-03-1.96752956E-03-2.82419302E-03-3.76227861E-03-4.79996164E-0311111
-5.19892375E-03-5.40344480E-03-5.57766135E-03-5.63448946E-03-5.90487278E-0311111
-5.91839386E-03-6.09790084E-03-6.20395420E-03-6.50615748E-03-6.54309260E-0311111
-6.92852458E-03-6.99488415E-03-7.36790450E-03-7.59059884E-03-7.87065639E-0311111
-7.89643131E-03-8.06568674E-03-8.44842430E-03-8.56684933E-03-8.96048160E-0311111
-9.11555727E-03-9.34674415E-03-9.64976680E-03-9.88953526E-03-9.93748766E-0311111
-1.01710347E-02-1.03682796E-02-1.04079791E-02-1.06169472E-02-1.08005647E-0211111
-1.09021263E-02-1.09397845E-02-9.37544559E-03 4.64288307E-02 1.06898251E-0111111
 1.09303068E-01 1.45619298E-01 2.16757642E-01 3.18245637E-01 3.59312715E-0111111
 4.85566455E-01 6.26267098E-01 8.26941220E-01 9.99980167E-01 1.18475391E+0011111
 1.48080219E+00 1.70486405E+00 1.94169114E+00 2.20651028E+00 2.77237405E+0011111
 3.37059171E+00 3.69343696E+00 4.08813452E+00 4.88701638E+00 5.67989818E+0011111
 6.55673450E+00 7.07754747E+00 7.57522506E+00 9.62244625E+00 1.26794275E+0111111
 1.32538406E+01 1.40709427E+01 1.88292312E+01 2.44976062E+01 2.53316372E+0111111
 2.62525400E+01 3.54924111E+01 4.82452159E+01 4.94702186E+01 5.02048681E+0111111
 7.70796857E+01 1.11169084E+02 1.12603763E+02 1.14126345E+02 2.09175972E+0211111
 3.41733954E+02 3.47498030E+02 3.53188811E+02 6.65219860E+02 1.13187998E+0311111
 1.15264588E+03 1.17567380E+03 2.30764733E+03 3.78775534E+03 3.85787801E+0311111
 3.92792403E+03 7.95338963E+03 1.34596191E+04 1.36592857E+04 1.38450184E+0411111
 3.31946193E+04 6.06859044E+04 6.10688540E+04 6.16123815E+04 1.04138133E+0511111
```

DISTRIBUTION:

4 Lawrence Livermore National Laboratory
Phil Sterne
Cristine Wu
Lorin Benedict
Eric Schwegler

2 Los Alamos National Laboratory
Scott Crockett
Carl Greeff

1 MS 1323 Erik Strack, 1443
1 MS 1323 John Carpenter, 1443
1 MS 1190 Keith Matzen, 1600
1 MS 1189 Mark Hermann, 1640
1 MS 1189 Thomas Mattsson, 1641
1 MS 1189 Kyle Cochrane, 1641
1 MS 1189 Dawn Flicker, 1646
1 MS 1195 Seth Root, 1646
1 MS 0899 Technical Library, 9536 (electronic copy)

Sandia National Laboratories